

Lappeenranta-Lahti University of Technology

School of Energy Systems

BH10A1101 Master's Thesis

Development of a Bubbling Fluidised Bed Furnace Model

Examiners: Prof. Timo Hyppänen, D.Sc. Jouni Ritvanen

Supervisor: M.Sc. Jouni Miettinen

Varkaus, 6.4.2020

Markus Secomandi

ABSTRACT

Lappeenranta-Lahti University of Technology

School of Energy Systems

Markus Secomandi

Development of a Bubbling Fluidised Bed Furnace Model

Master's thesis 2020

89 pages, 32 figures, 5 tables

Examiners: Professor Timo Hyppänen

D.Sc. Jouni Ritvanen

Supervisor: M.Sc. Jouni Miettinen

Keywords: bubbling, fluidised, bed, furnace, model

The main objective of this work was to further develop an existing bubbling fluidised bed furnace model by improving the accuracy of its predicted temperature profile to a level that would allow it to be used in determining the gas residence times for waste incineration plants and the height of ammonia injection levels in a furnace in both full and part-load runs.

The work focused on modelling the mixing of staged air injections and thus improving the heat release profile generated. Other aspects studied were the measurement error due to radiation between a thermocouple and furnace walls, and the estimation of unburnt fuel leaving the furnace area. Finally, the model was validated against the most up-to-date data available.

The objectives of the thesis were accomplished, with substantial improvements to the accuracy of the temperature profile achieved. Suggestions for future improvements were also given.

TIIVISTELMÄ

Lappeenrannan–Lahden teknillinen yliopisto

School of Energy Systems

Markus Secomandi

Leijukerroskattilan mallin kehitystyö

Diplomityö 2020

89 sivua, 32 kuvaa, 5 taulukkoa

Tarkastajat: Professori Timo Hyppänen

TkT Jouni Ritvanen

Ohjaaja: DI Jouni Miettinen

Hakusanat: leijupeti, kupla, tulipesä, malli

Työn päätarkoitus oli kehittää olemassaolevaa leijukerroskattilan mallia siten, että ennustettu lämpötilaprofiili olisi tarpeeksi tarkka, jotta sen avulla voitaisiin arvioida tulipesän ammoniakinsyöttötason koron ja täyttyvätkö jätteenpolttolaitoksille asetetut savukaasujen viipymäaika-vaatimukset sekä täydellä kuormalla että osakuormalla.

Kehitystyö keskittyi ilmansyöttöjen sekoittumisen mallintamiseen ja siten myös tarkemman palamisprofiilin ennustamiseen. Muita tarkasteltuja asioita olivat termoelementin ja tulipesän pintojen välisen säteilyn aiheuttaman mittausvirheen sekä palamattoman polttoaineen määrän arviointi. Lopuksi malli validoitiin vertaamalla saatuja tuloksia mittaustuloksiin.

Työn tavoitteisiin päästiin, ja mallin ennustama lämpötilaprofiili on tarkempi. Mallille listattiin myös kehitysehdotuksia.

ACKNOWLEDGEMENTS

This master's thesis was written in the Research and Development Centre of Sumitomo SHI FW in Varkaus between August 2019 and February 2020.

I would like to thank my supervisor, M.Sc. Jouni Miettinen for his invaluable guidance during this thesis, as well as Professor Timo Hyppänen and M.Sc. Ari Kettunen for their precious advice and the opportunity to work with such an interesting subject.

Finally, I would like to thank my friends and family for their support over the years.

Varkaus, April 6, 2020

Markus Secomandi

TABLE OF CONTENTS

| | |
|---|-----------|
| ABSTRACT | 2 |
| TIIVISTELMÄ | 3 |
| ACKNOWLEDGEMENTS | 4 |
| TABLE OF CONTENTS | 5 |
| NOMENCLATURE | 7 |
| 1 INTRODUCTION | 13 |
| 2 LITERATURE SURVEY | 14 |
| 2.1 Fluidisation..... | 14 |
| 2.1.1 Terminal velocity | 14 |
| 2.1.2 Minimum fluidisation | 16 |
| 2.1.3 Entrainment and elutriation of solids | 18 |
| 2.1.4 Fluidisation regimes | 20 |
| 2.1.5 Geldart classification of powders..... | 23 |
| 2.1.6 Industrial application..... | 24 |
| 2.2 Fluidised bed combustion..... | 25 |
| 2.2.1 Fuels | 25 |
| 2.2.2 Combustion process | 26 |
| 2.3 Heat transfer in BFB furnaces | 27 |
| 2.3.1 Bed area heat transfer..... | 27 |
| 2.3.2 Freeboard heat transfer..... | 29 |
| 2.4 Mixing | 32 |
| 2.4.1 Bed area mixing | 32 |
| 2.4.2 Freeboard mixing | 34 |
| 2.5 Existing models | 38 |
| 2.5.1 Mixing of a row of jets with a confined crossflow | 38 |
| 2.5.2 Comprehensive simulation program for fluidised beds | 41 |

| | | |
|----------|--|-----------|
| 3 | THE BFB FURNACE MODEL | 44 |
| 3.1 | Principles | 44 |
| 3.2 | Heat and mass balances | 46 |
| 3.3 | Entrainment | 47 |
| 3.4 | Gas absorption coefficient | 48 |
| 3.5 | Heat release | 48 |
| 3.6 | Moisture evaporation | 50 |
| 3.7 | Convection | 51 |
| 3.8 | Radiation | 52 |
| 4 | MODEL DEVELOPMENT | 56 |
| 4.1 | Thermocouple measurement error | 56 |
| 4.2 | Afterburning | 58 |
| 4.2.1 | Implementation as user input | 58 |
| 4.2.2 | Cases used in validation | 59 |
| 4.2.3 | Estimation of afterburning | 60 |
| 4.3 | Splitting of secondary air injection | 62 |
| 4.4 | Heat release function | 65 |
| 4.4.1 | The fuel-to-air factor | 69 |
| 4.4.2 | Mixing rate | 73 |
| 4.4.3 | Entrained fuel combustion | 75 |
| 4.5 | Gas absorptivity correlation | 75 |
| 4.5.1 | Comparison with entrainment correlations | 77 |
| 5 | RESULTS | 81 |
| 6 | SUMMARY | 86 |
| | REFERENCES | 87 |

NOMENCLATURE

Roman alphabet

| | | |
|-----------------|---|-------------------|
| A | area | $[m^2]$ |
| a | empirical parameter, gas absorptivity | $[-, 1/m]$ |
| a_{f1} | empirical constant | $[1/m]$ |
| B | solid loading | $[kg/m^3]$ |
| b_{0i} | empirical parameter | $[-]$ |
| b_{li} | empirical parameter | $[1/K]$ |
| C | mixing coefficient | $[-]$ |
| C_D | drag coefficient | $[-]$ |
| c_p | specific heat capacity | $[J/kgK]$ |
| D | diameter | $[m]$ |
| d | inlet diameter | $[m]$ |
| E | emitted power | $[W]$ |
| F | force, solids entrainment rate, fuel-to-air ratio | $[N, kg/m^2s, -]$ |
| F_∞ | solids elutriation rate | $[kg/m^2s]$ |
| f | heat release coefficient | $[-]$ |
| g | gravitational constant | $[m/s^2]$ |
| \overline{gg} | gas-gas direct exchange area | $[m^2]$ |
| \overline{gs} | gas-surface direct exchange area | $[m^2]$ |
| H | duct height | $[m]$ |
| ΔH_0 | reaction enthalpy | $[J/mol]$ |
| h | convective heat transfer coefficient | $[W/m^2K]$ |

| | | |
|------------------|---------------------------------------|---------------------|
| I | empirical parameter | [-] |
| J | momentum-flux ratio, radiosity | [-, W] |
| k | thermal conductivity | [W/mK] |
| k_{Gi} | volumetric gas absorption coefficient | [1/mbar] |
| k_{Ri} | empirical parameter | [m ² /K] |
| L | height | [m] |
| l | latent heat of evaporation | [J/kg] |
| m | mass | [kg] |
| N | number, amount | [-] |
| p | pressure, partial pressure | [Pa, bar] |
| Q | heat power | [W] |
| \bar{Q}_{abs} | mean relative effective cross-section | [-] |
| q_V | volumetric flow | [m ³ /s] |
| q_m | mass flow | [kg/s] |
| q'' | heat flux | [W/m ²] |
| S | spacing, traversed distance | [m] |
| s | share | [-] |
| s_{eq} | equivalent beam length | [m] |
| $\bar{s}\bar{s}$ | surface-surface direct exchange area | [m ²] |
| T | temperature | [K, °C] |
| u | velocity | [m/s] |
| V | volume | [m ³] |
| v | flow velocity | [m/s] |

| | | |
|-----------|---|--------|
| X | circularity, empirical coefficient | [-] |
| x | mass fraction, downstream distance | [-, m] |
| \bar{x} | particle mean diameter | [m] |
| y | distance from inlet wall, reactant quantity | [m, -] |
| z | height above grid | [m] |

Greek alphabet

| | | |
|---------------|------------------------------|------------------------------------|
| α | heat transfer coefficient | [W/m ² K] |
| Δ | difference | [-] |
| δ_b | bubble phase volume fraction | [-] |
| ε | voidage | [-] |
| θ | dimensionless scalar, angle | [-] |
| λ | air coefficient | [-] |
| μ | dynamic viscosity | [Pa s] |
| π | mathematical constant | [-] |
| ρ | density | [kg/m ³] |
| σ | Stefan-Boltzmann constant | [W/m ² K ⁴] |
| ϕ | sphericity | [-] |
| ψ | particle shape factor | [-] |

Dimensionless numbers

| | |
|----|-------------------|
| Ar | Archimedes number |
| Nu | Nusselt number |

Pr Prandtl number

Re Reynolds number

Superscripts

- injection side

+ side opposite to injection

Subscripts

0 initial

A ash

B buoyant

b bed, bubble

C char

c cross-section, cross-flow, central profile

comb combustion

conv convection

D drag

d grid orifice diameter

e electric output

entr entrained

f fuel, fluid

FEGT furnace exit gas temperature

FEGT,eb FEGT matched to boiler energy balance

fg flue gas

freeb freeboard

| | |
|------|--------------------------------------|
| furn | furnace |
| G | gravity |
| gc | gas, convective |
| ht | heat transfer |
| j | jet |
| max | maximum |
| min | minimum |
| mf | minimum fluidisation |
| opt | optimal |
| p | particle |
| pc | post-combustion, particle convective |
| R | soot |
| r | radiation |
| ref | refractory |
| refl | reflected |
| rg | recirculation gas |
| S | gas-solids suspension |
| s | slip (velocity) |
| sens | sensible |
| sp | sphere |
| st | stoichiometric |
| t | terminal (velocity) |
| tc | thermocouple |
| th | thermal output |

tot total

w wall

Abbreviations

BFB bubbling fluidised bed

CFB circulating fluidised bed

CSFB comprehensive simulation program for fluidised beds

FEGT furnace exit gas temperature

FR forest residue

LHV lower heating value

MAE mean absolute error

MBE mean bias error

SD standard deviation

1 INTRODUCTION

With the increasing popularity of alternative fuels such as different residues and wastes, a higher emphasis is placed on the ability of a furnace to burn low-quality fuels. Bubbling fluidised bed (BFB) firing is a common choice when burning high moisture and high ash fuels due to its insensitivity to fuel quality. Additionally, its ability to reduce NO_x emissions through ammonia injection in the furnace helps in meeting increasingly strict environmental regulations.

However, the injection of ammonia must be done at the right temperature for it to be effective, which means that the temperature profile of the furnace must be known when choosing the injection level height. Similarly, the EU Directive 200/76/EC requires that the gas temperature of waste incineration units be kept at a temperature of 850 °C or higher for a minimum of two seconds after the last air injection to ensure complete combustion. As such, the ability to predict the temperature profile of a given furnace with sufficient accuracy is important.

A BFB furnace model was developed over the course of two previous master's theses by Jani Ikonen (2004) and Juha Keltanen (2007). The objective of this work is to further develop the existing model by improving the accuracy of the generated temperature profile for both full and part load situations to allow it to be used in the evaluation of ammonia injection levels and of hot gas residence times.

The development work was done by studying measurement data and the literature available on the subject and applying this knowledge to produce a more accurate model. Aspects studied include the measurement error of a thermocouple due to radiation, the spreading and mixing of staged air injections, the combustion of fuel in the furnace, and the estimation of the gas absorptivity of the flue gases and its effect on thermal radiation in the furnace. Finally, the model was validated by comparing the obtained results with the most up-to-date measurement data available.

2 LITERATURE SURVEY

In this chapter, key phenomena present in bubbling fluidised bed combustors are covered, followed by an overview of two models found in literature that are related to the present work.

2.1 Fluidisation

A typical body of solid particles is able to partly resist the force of gravity due to the friction force between particles. Sand dunes, for example, can keep their characteristic shape despite being pulled down by gravity, while liquid water bodies at rest are always flat. This interparticular friction is, in most cases, caused by gravity compressing the bed of particles. By forcing a fluid flow through the bed of solids in the direction opposite to gravity, the gravitational force can be compensated by the drag force exerted by the fluid on the particles. This greatly reduces the tensile stresses acting on the solids, allowing them to move freely with relation to one another in a state similar to that of a fluid, i.e. in a fluidised state. (Scala 2013, p.3.)

2.1.1 Terminal velocity

The gravitational force acting on a solid particle is given by

$$F_G = m_p g \quad (1)$$

where m_p is the mass of the particle
 g is the gravitational constant

If this particle is placed in an upwards fluid flow, this gravitational force is at least partially mitigated by the buoyancy F_B and drag F_D forces, given in

$$F_B = V_p \rho_f g \quad (2)$$

where V_p is the volume occupied by the particle
 ρ_f is the density of the fluid

and

$$F_D = C_D A \frac{1}{2} \rho_f (u - u_p)^2 \quad (3)$$

where C_D is the drag coefficient
 A is the particle reference area, i.e. the largest area occupied by the particle in a plane normal to the flow direction
 u is the fluid flow velocity
 u_p is the particle velocity

By assuming the positive force direction to be downwards, these forces can be combined and expressed as

$$F_{\text{tot}} = V_p (\rho_p - \rho_f) g - C_D A \frac{1}{2} \rho_f (u - u_p)^2 \quad (4)$$

The flow velocity difference between the fluid and a particle is known as the slip velocity u_s and is defined as

$$u_s = u - u_p \quad (5)$$

The terminal velocity u_t of a particle in relation to the fluid can be found by solving u in equation 4 with the knowledge that the sum of forces exerted on the particle must be zero, yielding

$$u_t = \sqrt{\frac{2V_p(\rho_p - \rho_f)g}{AC_D\rho_f}} \quad (6)$$

The main difficulty in determining the terminal velocity of a particle is in the drag coefficient. For a spherical particle, the drag coefficient is only a function of its Reynolds number Re (Dioguardi & Mele, 2015)

$$Re = \frac{\rho_f u_t d_p}{\mu} \quad (7)$$

The drag coefficient of a sphere can be calculated according to (Scala 2013, p. 56)

$$C_D = \begin{cases} \frac{24}{Re_p} & \text{for } Re_p < 2 \\ \frac{18.5}{Re_p^{0.6}} & \text{for } 2 < Re_p < 500 \\ 0.44 & \text{for } 500 < Re_p < 2 \cdot 10^5 \end{cases} \quad (8)$$

However, for an irregularly shaped particle, the drag coefficient is a function of Reynolds number and shape, but the shape of a particle can be defined in many different ways. The method used by Dioguardi & Mele (2015) used the particle shape factor Ψ , which is defined as the ratio between sphericity ϕ and circularity X . The particle sphericity is defined as

$$\phi = A_{sp}/A_p \quad (9)$$

where A_{sp} is the surface area of a sphere of diameter d_p
 A_p is the particle surface area

and the circularity X is defined as the ratio between the ratio of the maximum projection perimeter of a particle to the perimeter of the circle equivalent to the maximum projection area. Their correlation for the drag coefficient of an irregularly shaped particle is

$$C_D = \frac{C_{D,sphere}}{Re^2 \Psi^{exp}} \left(\frac{Re}{1.1883} \right)^{\frac{1}{0.4826}} \quad (10)$$

where exp is equal to $Re^{-0.23}$ for $0 < Re < 50$
or $Re^{0.05}$ for $50 < Re < 10\,000$

2.1.2 Minimum fluidisation

For a single, small particle in a plug flow, the slip velocity is practically the same as the average flow velocity. In fluidised systems, this average flow velocity is known as the fluidisation velocity and is defined as

$$u_f = \frac{q_V}{A_c} \quad (11)$$

where q_V is the volumetric fluid flow
 A_c is the cross-sectional area of the flow

For a bed of particles, the slip velocity is higher than the fluidising velocity due to the reduced cross-sectional area caused by the blocking effect of particles. This means that the gravitational force exerted on these particles can be balanced by the fluid drag force at a fluidisation velocity significantly lower than the terminal velocity of an individual particle. The minimum fluidisation velocity at which the system is in this state of equilibrium is called the minimum fluidisation velocity u_{mf} . In this state of minimum fluidisation, the bed appears to experience a phase change from solid to fluid-like, as the particles lose contact with one another and friction is lost. (Scala 2013, pp. 6-7.)

According to Scala (2013, p.9), the macroscopic force balance of the bed at the state of minimum fluidisation can be written as

$$(1 - \varepsilon)(\rho_p - \rho_f)gL_bA_c = \Delta pA_c \quad (12)$$

where Δp is the pressure drop over the bed
 L_b is the height of the bed
 ε is the bed voidage, defined as

$$\varepsilon = 1 - \Sigma V_p / V_b \quad (13)$$

where ΣV_p is the total volume occupied by particles
 V_b is the total volume of the bed

The pressure drop can be calculated by the Ergun correlation

$$\frac{\Delta p}{L} = 150 \frac{(1 - \varepsilon)^2}{\varepsilon^3} \frac{\mu u_f}{\phi^2 d_p^2} + 1.75 \frac{1 - \varepsilon}{\varepsilon^3} \frac{\rho_f u_f^2}{\phi d_p} \quad (14)$$

where d_p is the diameter of a sphere with the same volume as particle
 μ is the fluid dynamic viscosity
 ϕ is the particle sphericity

If equations 12 and 14 are combined, the following Wen-Yu correlation is obtained (Scala 2013, p. 80)

$$150 \frac{(1 - \varepsilon_{mf})^2}{\varepsilon_{mf}^3 \phi^2} \text{Re}_{mf} + 1.75 \frac{1 - \varepsilon_{mf}}{\varepsilon_{mf}^3 \phi} \text{Re}_{mf}^2 = \text{Ar} \quad (15)$$

where ε_{mf} is the bed voidage at minimum fluidisation
 Re_{mf} is the Reynolds number at minimum fluidisation
 Ar is the Archimedes number, given by

$$\text{Ar} = \frac{d_p^3 \rho_f (\rho_p - \rho_f) g}{\mu} \quad (16)$$

Since the particle shape factor ϕ and bed voidage ε_{mf} are difficult to determine, Wen and Yu suggested the following empirical correlation to estimate u_{mf} with an error of about 34 % (Scala 2013, p. 80)

$$\text{Re}_{mf} = [33.7^2 + 0.0408 \text{Ar}]^{0.5} - 33.7 \quad (17)$$

The minimum fluidisation velocity u_{mf} can then be solved using the definition of the Reynolds number Re

$$\text{Re}_{mf} = \frac{d_p u_{mf} \rho_f}{\mu} \quad (18)$$

If the fluidisation velocity is increased past the minimum fluidisation velocity, the increased drag force acting on the particles causes the bed to expand. This increases the spacing between particles, which in turn results in a lower interstitial fluid flow velocity, bringing the net force back to balance. If the fluidisation velocity is high enough, close to the particle terminal velocity, further bed expansion is incapable of balancing the net forces exerted on the bed particles. This causes the particles themselves to accelerate with the flow, until the slip velocity between the fluid and particles is low enough to return the system to a state of equilibrium. The particles are then carried away with the fluid flow or entrained.

2.1.3 Entrainment and elutriation of solids

The entrainment of bed material and fuel particles means there is a concentration profile of solids above the bed surface. Knowledge of how this solids concentration varies above

the bed is important, as the concentration of char and soot above the bed, for instance, has a significant effect on the radiative properties of the flue gas suspension and on the char combustion profile. Wen and Chen (1982) suggested the following method for estimating the solids load profile in the freeboard.

The total rate of entrained solids F_0 leaving the surface of a bubbling fluidised bed due to bubble eruptions can be calculated by

$$\frac{F_0}{A_c D_{bH}} = 3.07 \cdot 10^{-9} \frac{\rho_f^{3.5} g^{0.5}}{\mu_f^{2.5}} (u_f - u_{mf})^{2.5} \text{ kg/m}^5 \text{ s} \quad (19)$$

The bubble diameter at the bed surface D_{bH} can be estimated by using the following correlation by Darton et al. (1977) for the equivalent diameter of a bubble D_e

$$D_e = 0.54 (u_f - u_{mf})^{0.4} (z + 4\sqrt{A_d})^{0.8} g^{-0.2} \quad (20)$$

where z is the height above the grid
 A_d is the area of a single grid orifice

The entrained solids load profile with height z above the bed surface is given by

$$F(z) = F_\infty + (F_0 - F_\infty) \exp(-a_{f1} z) \quad (21)$$

where a_{f1} is an empirical constant of 4.0 1/m
 F_∞ is the fines elutriation rate, given by

$$F_\infty = \sum_i \rho_p (1 - \varepsilon_i) (u_f - u_{ti}) A_c x_i \quad (22)$$

where x_i is the mass fraction of particles of diameter d_{pi}
 u_{ti} is the terminal velocity of particles of size d_{pi}
 ε_i is the freeboard voidage for the elutriation of particles of size d_{pi} , given by

$$\varepsilon_i = \left[1 + \frac{\lambda_e (u_f - u_{ti})^2}{2gD} \right]^{-\frac{1}{4.7}} \quad (23)$$

where D is the bed diameter

and λ_e is solved from

$$\frac{\lambda_e \rho_p}{d_{pi}^2} \left(\frac{\mu_f}{\rho_f} \right)^{2.5} = 5.17 \text{Re}_p^{-1.5} D^2 \quad \text{for } \text{Re}_p < 2.38/D \quad (24)$$

$$\frac{\lambda_e \rho_p}{d_{pi}^2} \left(\frac{\mu_f}{\rho_f} \right)^{2.5} = 12.3 \text{Re}_p^{-2.5} D \quad \text{for } \text{Re}_p > 2.38/D \quad (25)$$

where Re_p is the particle Reynolds number.

However, a recent review of entrainment correlations by Chew et al. (2015) found that these produced results that differed by up to 20 orders of magnitude, meaning their validity is limited to the range of tested parameters, which are often not reported.

2.1.4 Fluidisation regimes

A fluidised bed consists of a layer of bed material, usually sand, on top of a grid through which air is fed. This fluidising air causes the bed material to behave in different ways, depending on the fluidising velocity. These different fluidisation regimes are summarised in Figure 1. (Spliethoff, 2010, p. 263.)

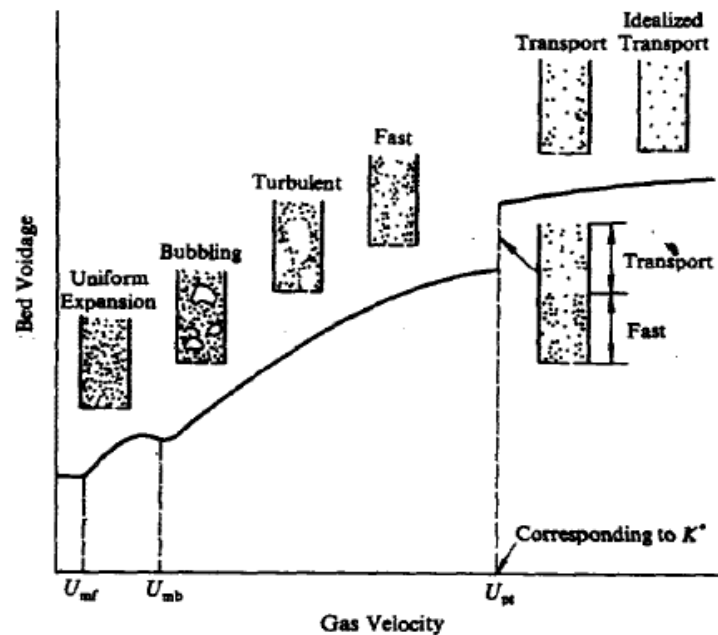


Figure 1. Fluidisation regimes (Li & Kwauk, 1994)

At low velocities, the air simply flows through the bed without much effect, but part of the weight of the particles is still supported by the counter force exerted by air drag (Li & Kwauk, 1994, p. 1). A system like this is called a fixed bed.

As the air velocity approaches minimum fluidisation velocity, the fraction of the weight of the bed particles supported by air drag approaches unity. At this state of minimum fluidisation, the bed is suspended by the air flow, and interparticular spacing begins to increase. Internal friction caused by the compressing effect of gravity on the bed is significantly reduced, and the suspended solids are distributed homogeneously over the expanded bed. (Spliethoff, 2010, p. 264; Horio, 2010; Li & Kwauk, 1994, p. 1.)

Further increasing the fluidisation velocity causes the bed to continue to expand to allow the excess air to pass, yet it will retain its homogeneous particle distribution until the minimum bubbling velocity is reached. For sand typically used in bubbling fluidised beds, this expansion range is small. If the fluidising velocity is increased further, the flow starts to bubble and becomes heterogeneous. This two-phase structure consists of a continuous dense phase, with bubbles of a dilute phase passing through. In the dense phase, gas and solids are mixed homogeneously in a state akin to the one of minimum fluidisation, whereas the dilute phase consists mostly of gas. Further increasing the fluidisation velocity causes the excess gas to pass through the bed in the form of bubbles, i.e., it increases the proportion of the dilute phase in relation to the dense phase. This causes the overall density of the bed to decrease, and consequently results in further bed expansion that is proportional to the amount of excess gas fed. The coalescence of gas bubbles as they travel upwards results in larger bubbles in the core region of the fluidising vessel, and consequently in a denser near-wall region. (Geldart, 1973; Li & Kwauk, 1994, p. 2; Spliethoff, 2010 p. 264.)

As the fluidisation velocity is increased past the point where the dilute phase occupies a volume greater than the dense phase, the two phases gradually become inverted, i.e., one would have a continuous dilute phase with a discontinuous dense phase in the form of strands or clusters in a mode called fast fluidisation. The transition between bubbling and fast fluidisation is often named turbulent fluidisation and is characterised by highly deformed bubbles accompanied by transient strands and clusters. In these high-velocity

types of fluidisation, entrainment of bed material happens to a great extent, and a constant inventory cannot be maintained without a recirculation system. However, the formation of bubbles, clusters and strands, along with the higher solids concentration and back-flow in the near-wall region greatly reduces the entrainment of particles by presenting the fluidising gas with distinct low-resistance and high-resistance paths to take, as shown in Figure 2. This results in a lower gas velocity through the dense phase than would be seen in a homogeneous fluidised system, and consequently, slip velocities between gas and clusters significantly higher than the terminal velocity of individual particles can be seen in heterogeneous systems, with a much lower level of entrainment of solids. (Li & Kwauk, 1994, pp. 4–6.)

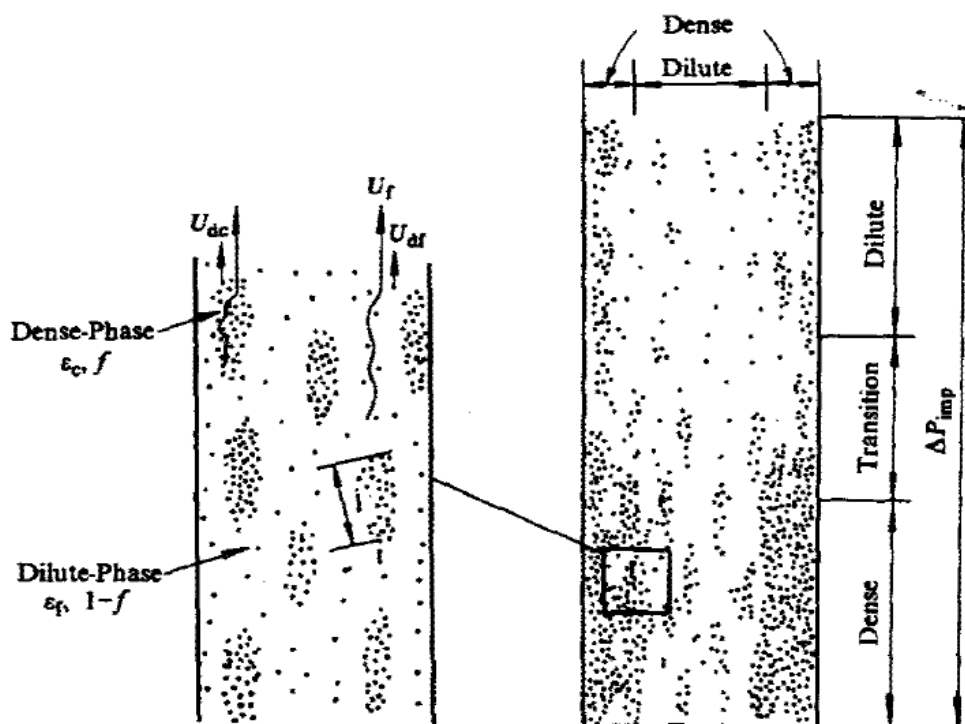


Figure 2. Heterogeneous flow structures present in fast fluidisation (Li & Kwauk, 1994)

If the fluidising velocity is greater than the pneumatic transport velocity, a sudden change in bed structure happens and the dilute phase occupies the entire volume, bringing the system back to a state of relative homogeneity. The homogeneity of the system increases as the gas velocity is further increased. (Li & Kwauk, 1994, pp. 5–6.)

2.1.5 Geldart classification of powders

The type of solid particles or powder used in a fluidised system has a significant effect on how the solids in question behave when subjected to fluidising conditions. In 1973, D. Geldart published a method for characterising powders according to how they behave when fluidised by air. According to this method, solid particles would be divided in four groups, named A to D, based on their density and mean particle size. These four groups are shown in Figure 3 below. (Geldart, 1973.)

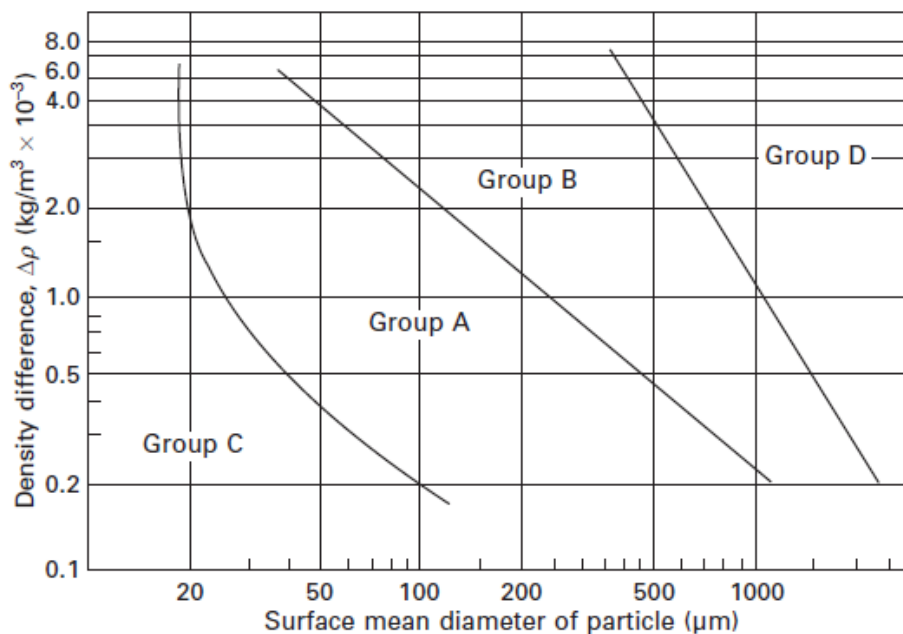


Figure 3. Particle characterisation by Geldart (Scala 2013, p. 84)

Materials of group A have small mean particle size in the order of 30–150 μm and/or a low density, typically under 1400 kg/m^3 . When fluidised, a bed of this type of powder expands considerably before starting to bubble, resulting in a collapse in bed height past this threshold. An example of a group A powder would be cracking catalyst. (Geldart 1973, Scala p. 84.)

A bed of particles of group B starts to bubble shortly after reaching the minimum fluidisation velocity, which means little expansion happens. Typical particle sizes are around 40–500 μm and the densities usually vary between $1400\text{--}4000 \text{ kg/m}^3$, sand being a common example. (Geldart 1973, Scala p. 84.)

The powders of group C are fine, with diameters smaller than 30 μm . They are cohesive and difficult to fluidise due to their small particle size and strong interparticular forces, which causes the bed to be lifted as a plug or small channels to be formed if fluidisation is attempted. An example of such a powder is flour. (Geldart 1973, Scala p. 84.)

Group D contains large or dense particles, with diameters larger than 1 mm and/or density higher than 1 500 kg/m^3 . Relatively sticky particles can still be fluidised due to lesser particle contact. (Geldart 1973, Scala p. 84.)

2.1.6 Industrial application

The first time fluidised bed technology was used industrially was in the 1920's for coal gasification. The development of bubbling fluidised bed (BFB) combustion followed in the 1960's, with commercial applications being seen in the following decade. The capacity of BFB systems has since increased, from the first 20 MW_{th} boilers seen in the early 1970's to plants like the 350 MW_e Takehara unit in Japan. However, most large fluidised bed units currently built are circulating fluidised bed (CFB) boilers, with BFBs being preferred for low capacity applications or when using fuels of a low heating value. (Spliethoff 2010, pp. 263-266.)

Bubbling fluidised bed boilers are typically operated with fluidising velocities in the range of 1–3 m/s and a bed height of roughly 1–1.5 m. The bed has a well-defined surface despite the constant bubbling, while the upper region, i.e. the freeboard, has a low concentration of solids. The region just above the bed, called the splash-zone, has a density higher than the rest of the freeboard due to the constant ejection of particles caused by bubble eruptions. Fuel is typically fed through chutes on the walls. Biomass-firing BFBs are operated in substoichiometric conditions in order to keep the bed temperature close to 800 $^{\circ}\text{C}$. The walls around the bed and splash areas are protected against erosion by a refractory layer. Secondary air staging is used to ensure proper mixing of oxygen with released volatile gases in the freeboard to reduce losses due to unburned fuel. The staged air injection causes the formation of a combustion zone above the lower secondary air levels, where the released volatiles are oxygenated. This combustion zone can have temperatures more than 300 $^{\circ}\text{C}$ higher than the bed temperature. The hot flue gases then

cool as they radiate heat to the membrane walls while travelling through the freeboard. (Spliethoff 2010, pp. 265-266; Koornneef et al., 2007.)

The fluidisation velocity of circulating fluidised beds is significantly higher, in the order of 3–10 m/s. The bed material used is much finer than that used in BFBs, which combined with the increased gas velocity results in a high level of entrainment of solids. There is no longer a clearly defined bed surface, and instead the solids concentration decreases steadily with height. Despite this decrease, the solids load in the upper parts of a CFB furnace can be as high as 10 kg/Nm³, compared to the load of roughly 50 g/Nm³ in a BFB freeboard. The high flux of solids circulating in a CFB due to entrainment and back-flow in locally denser areas results in efficient mixing throughout the entire reactor volume and a much more even temperature profile than seen in the freeboard of BFBs. (Koornneef et al., 2007, Spliethoff 2010.)

2.2 Fluidised bed combustion

Combustion in fluidised beds differs from other firing methods mainly due to the efficient solids mixing in the bed area and the high heat capacity of the bed. This results in a wider variety of fuels being viable for fluidised bed combustion, and in faster fuel conversion times in the bed.

2.2.1 Fuels

Fluidised bed furnaces are particularly well suited to burn heterogeneous fuels that are difficult to utilise efficiently in other ways. Such fuels are coals, peat, biomass, and different types of waste. (Scala 2013, pp. 320-321.)

Coals are fossil fuels with varying fixed carbon content, ranging from 80 % dry basis (d.b.) for anthracite, to as low as 25 % for lignite (Scala 2013, pp. 320–322). Due to the high fixed carbon content, they are not typically used in BFB furnaces, as the short gas residence time results in the losses due to unburned carbon being relatively high.

Biomass and peat are both relatively young fuels with a high volatile content and are commonly used in BFB boilers. Peat is essentially decaying plant matter too young to be

considered coal. Biomass is even younger and can be of vegetable or animal origin. Commonly used types of biomass are agricultural and forest residues, wood chips, and bark. (Scala 2013, pp. 320-321.)

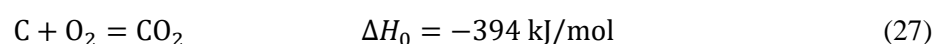
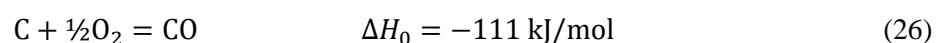
The distinction between waste and biomass varies from country to country, with some countries using the term biomass for all renewable organic matter (Spliethof 2010, p. 29). However, waste fuels are generally defined as residues from civil and industrial processes with a high enough heating value. These include refuse-derived fuel, sewage sludge, tyres, and paper and plastic waste. (Scala 2013, p. 321.)

2.2.2 Combustion process

The combustion process of a fuel particle starts as it is fed into the furnace and consists of four stages that can happen simultaneously or sequentially. According to Scala (2013, p. 325) warming happens quickly due to the relatively low Biot numbers of the particles, which is followed by drying at temperatures in the 100–200 °C range, but other sources have reported that biomass particles on the scale of a few millimetres can no longer be considered to be thermally thin, i.e. assuming their inner temperature gradient to be non-existent produces significantly different results (Momenikouchaksaraei, 2013). Drying times of wood particles are of the order of 40 seconds for particles with a diameter of 10 mm in 1050 K air (Haberle, 2018), but this should be faster in the bed, with Scala (2013, p. 326) reporting that typical drying times are in the order of a few seconds.

Devolatilisation happens when the fuel particle temperature is between 400–700 °C, during which the hydrogen-rich matter found in the solid matrix is broken into gaseous compounds. This process is slightly endothermic, and the decrease in fuel solid mass can cause the fuel particles to shrink and fragment. This process typically lasts between 10 and 100 seconds but is dependent on the fuel type and particle size. (Scala 2013, p. 326.)

Finally, the remaining char particles are oxidised until only ash is left, producing mainly carbon monoxide (CO) and dioxide (CO₂) according to the following equations



The ratio of CO to CO₂ produced can have a significant effect on the heat balance around the particles, and consequently on the bed area, since the partial oxidation of carbon into CO only releases a fraction of its potential heat. The char conversion times are typically around of the order of 100–1000 s. (Scala 2013, pp. 326, 335)

The fuel particle size has a significant effect on its conversion time, with Haberle (2018) reporting that the overall conversion time was roughly proportional to the square of the particle diameter d_p for particles with $10 \text{ mm} < d_p < 40 \text{ mm}$. However, if the char particles experience attrition and cracking in the fluidised bed, their overall conversion times would be harder to estimate.

2.3 Heat transfer in BFB furnaces

Heat transfer inside a furnace is a complex phenomenon, which is mainly dependent of heat convection with gases and solids, heat released via chemical reactions, and radiation between surfaces, gases, and suspended particles. The heat transfer in a BFB furnace can be split into two parts, that of the freeboard, and that of the bed region. Heat transfer in the bed area is dominated by gas and particle convection, while heat transfer in the upper regions of the furnace consists mostly of radiation between different elements.

2.3.1 Bed area heat transfer

Heat transfer in a bubbling fluidised bed consists of three main processes, namely the diffusion and convection with gas, diffusion of heat through contact between particles, and radiation.

For a wall immersed in a bubbling fluidised bed, the overall heat transfer coefficient h can be written as a sum of the processes listed above (Scala 2013, p.181.)

$$h = (h_{gc} + h_{pc})(1 - \delta_b) + h_b \delta_b + h_r \quad (28)$$

where

| | |
|----------|--|
| h_{gc} | is the gas convective heat transfer coefficient |
| h_{pc} | is the particle convective heat transfer coefficient |
| h_r | is the radiative heat transfer coefficient |

h_b is the bubble convection heat transfer coefficient
 δ_b is the dilute phase (bubble) volume fraction

The overall heat transfer coefficient between bed and immersed surfaces has been widely studied due to its importance in many industrial applications. As can be seen in Figure 4, the heat transfer coefficient sees a sharp increase after the minimum fluidisation velocity is reached. This is due to the moving particles and the particle convective heat flow associated with it. As the fluidisation velocity is increased past an optimum velocity (u_{opt}), the heat transfer coefficient begins to decline. This is caused by the lower density of the bed as it expands. (VDI 2010, p. 1304.)

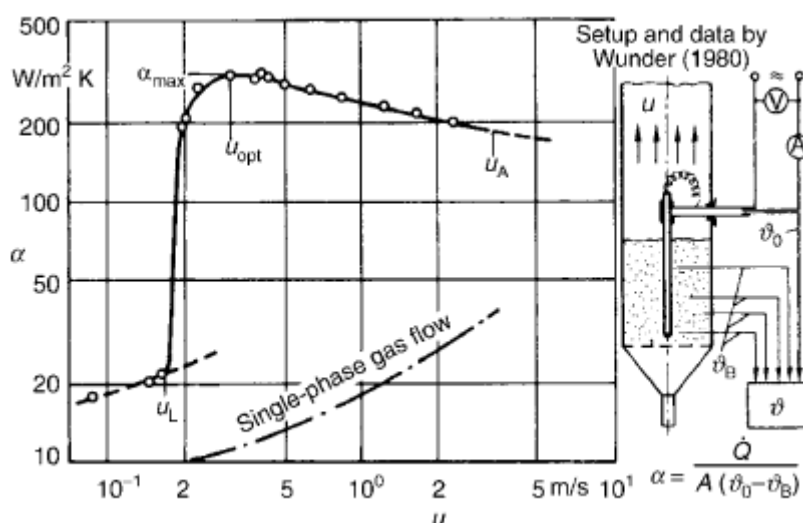


Figure 4. Overall heat transfer coefficient (α) between bed and an immersed surface as function of gas velocity (VDI 2010, p. 1304.)

Despite the high heat transfer coefficients between the bed and the surrounding walls, the thick refractory covering the tube walls of BFB furnaces results in significantly weaker overall bed-to-wall heat transfer. Because of this, a very accurate estimation of the overall heat transfer coefficient in the bed area is not necessary in this particular application.

In addition to the heat transfer between the bed and the surrounding walls, another heat transfer mechanism within the bed area is between the bed and the fluidising gas. On the one hand, as the fluidising gas enters the bottom of the bed, it is heated by the hot bed material, and on the other hand, the hot combustion gases heat the bed as the fuel burns

near the surface of the bed. Despite a short residence time in the bed area and the relatively low heat transfer coefficient (4–25 W/m²K) between the two phases, heat transfer between the two phases happens very quickly due to the large surface area of the bed material, and thermal balance between the fluidising air and the bed is reached close to the grid. Because of this, detailed modelling of the heat transfer between these two phases in the bed area is not important, and a simple energy balance is sufficient for most applications. (Scala 2013, p. 205.)

2.3.2 Freeboard heat transfer

Heat transfer in the freeboard of a BFB furnace is dominated by radiation, with the contribution of convection to the total heat being transferred to walls being in the order of 10 %.

The calculation of radiative heat transfer requires knowledge of the properties of the flue gas and particle mixture and of the walls, as the emission, absorption, reflection, and scattering of radiation must be computed. There is strong coupling between subsystems, as the temperature field, flow velocity field, and concentration fields of different species are heavily dependent on one another. It is usually not possible to predict the temperature field of a furnace, and instead it is solved based on the flow and heat release fields. In order to solve the whole system, the system is divided into finite volumes and surfaces, for which balance equations may be written and the interdependent fields solved iteratively. However, calculating the radiative heat exchange of a realistic furnace geometry is mathematically challenging, and the needed physical properties of all components present in a furnace are rarely completely known. Because of this, the heat transfer calculations in furnaces are simplified. (VDI 2010, p. 1001.)

The main components in the absorption and emission of radiation inside a furnace are water vapour, carbon dioxide, and suspended particles such as soot, char and ash. The radiation of solid elements like particles and membrane walls is not strongly dependent on the wavelength of radiation and these can be approximated as grey radiators. Water vapour and carbon dioxide are so-called narrow band radiators, as they exhibit largely

different radiative properties depending on wavelength, and this must be considered in the calculations for the obtained results to be accurate. (VDI 2010, p. 1002.)

In simplified calculations of radiation in a furnace, the only radiating elements in the flue gas suspension can be assumed to be water vapour and carbon dioxide with uniform partial pressures throughout the enclosure. These partial pressures can be obtained by assuming complete ideal combustion, if the fuel composition and excess air are known. Once the furnace geometry and partial pressures are known, the emissivities of these gases can be found in literature or matched to measurement results. One way to calculate the emissivity of a gas volume is as a weighted sum of exponential functions (VDI 2010, p. 1002.)

$$\varepsilon_G = \sum_{i=1}^3 a_i (1 - e^{-k_{Gi} p_G s_{eq}}) \quad (29)$$

where k_{Gi} is the volumetric gas absorption coefficient
 p_G is the partial gas pressure ($p_{H_2O} + p_{CO_2}$)
 s_{eq} is the equivalent beam length
 a_i is an empirical weighting parameter given by

$$a_i = b_{0i} + b_{1i} T_G \quad (30)$$

where b_{0i} and b_{1i} are empirical parameters
 T_G is the gas temperature in K

The values for the empirical parameters b_{0i} , b_{1i} and k_{Gi} are given in Table 1.

Table 1. Empirical parameters b_{0i} , b_{1i} , k_{Gi} and k_{Ri} for the gas and soot phases, total pressure 1 bar, $0.5 < p_{H_2O}/p_{CO_2} < 2$. (VDI 2010, p. 1002.)

| i | b_{0i} [-] | b_{1i} [1/K] | k_{Gi} [1/(m bar)] | k_{Ri} [m ² /K] |
|---|--------------|----------------|----------------------|------------------------------|
| 1 | 0.13 | +0.000265 | 0.0 | 3 460 |
| 2 | 0.595 | -0.000150 | 0.924 | 960 |
| 3 | 0.275 | -0.000115 | 25.907 | 960 |

The emissivity of the particle suspension consists of the emissivities of ash, soot, and char. For soot, the emissivity equation obtained is similar to the one for gases

$$\varepsilon_R = \sum_{i=1}^3 a_i (1 - e^{-k_{R,i} B_R s_{eq}}) \quad (31)$$

where B_R is the soot particle loading
 a_i is the same parameter used for the gas phase
 k_{Ri} is the emissivity coefficient given in Table 1. Empirical parameters b_{0i} , b_{1i} , k_{Gi} and k_{Ri} for the gas and soot phases, total pressure 1 bar, 0

For larger particles, such as char and ash, the particle size distribution must be taken into account. For a constant particle diameter, the emissivity equation of char takes the form

$$\varepsilon_C = 1 - \exp \left[-\bar{Q}_{abs,C} \frac{3}{2 \cdot \rho_C \cdot \bar{x}_C} B_C s_{eq} \right] \quad (32)$$

where $\bar{Q}_{abs,C}$ is the mean relative effective cross section for char particles, 0.8 – 1.0 for larger particles.
 ρ_C is the char particle density
 \bar{x}_C is the particle mean diameter
 B_C is the char particle loading

The ash emissivity ε_A can be calculated similarly, using $\bar{Q}_{abs,A} = 0.2$ instead.

Finally, if the particles are assumed to be grey radiators, the emissivity of the gas-solids suspension can be calculated

$$\varepsilon_S = 1 - (1 - \varepsilon_G)(1 - \varepsilon_R)(1 - \varepsilon_C)(1 - \varepsilon_A) \quad (33)$$

In the radiation of ash, soot, and char, estimating their mass loading (kg/m^3) proves to be a problem. This is the case especially for soot and char due to their highly heterogeneous loading in the furnace, with the highest concentrations being found at the flame core where the oxygen concentration is low, but a theory that would predict the formation of soot accurately has not been found. Additionally, soot and char can burn in areas with excess oxygen, given sufficient temperature and residence time, but this is strongly dependent on the furnace gas flow field and difficult to model. (VDI 2010, p. 1005.)

Once the suspension emissivity is known, the heat power emitted by a suspension volume to a surface can be written as

$$E_S = \varepsilon_S A \sigma T_S^4 \quad (34)$$

where σ is the Stefan-Boltzmann constant
 T_S is the suspension temperature
 A is the receiving surface area

2.4 Mixing

A major challenge in the modelling of bubbling fluidised bed furnaces is the mixing of oxygen and combustible gases, especially when burning fuels with a high volatile matter content such as biomass. According to Scala (2013, p. 335), the combustion of volatiles is not controlled by their kinetic reaction rates, but by their mixing with oxygen. Thus, a solid understanding of mixing is essential for the prediction of the heat release profile of a biomass furnace.

2.4.1 Bed area mixing

Ideally, fuel would spread and burn evenly across the furnace cross-section. However, practical experience shows that combustion of fuels with a high volatile content is significantly stratified (Scala 2013, p. 333.)

Bubbles are the main solids mixing mechanism in bubbling fluidised beds. This happens in three different ways. The first is via bubble wake transport, in which particles are pulled upwards in the wake of bubbles, and which is balanced by a downward drift of solids in the surrounding dense phase. This was found to mainly affect vertical mixing. (Olsson et al., 2012.)

Additionally, there is lateral exchange of bed material between neighbouring drifting columns, as well as the lateral dispersion of fuel due to ejection of particles caused by bubble eruptions, as is shown in Figure 5. According to Sette et al. (2014), overall mixing in the bubbling fluidised bed is limited primarily by lateral dispersion. This is because vertical mixing is faster than lateral mixing, due to the geometry of most commercial fluidised bed boilers, i.e. the bed being relatively shallow and wide.

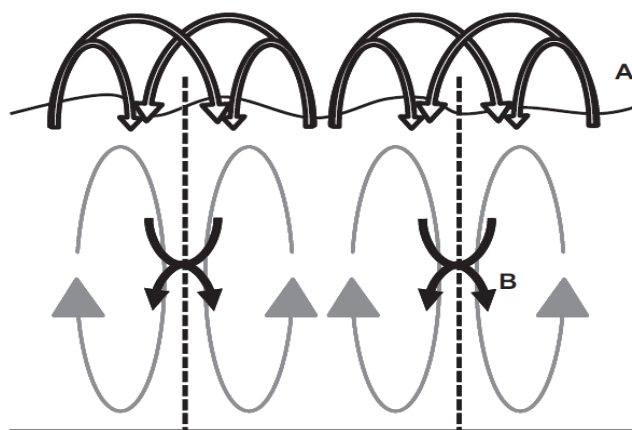


Figure 5. Lateral solids mixing via (A) bubble eruptions (B) exchange of material between vortices (Olsson et al., 2012)

According to a study by Solimene et al. (2012), the lateral mixing time of fuel particles smaller than 1 cm is longer than their devolatilisation time. This results in the volatile matter being released close to the fuel feeding points. Insufficient fuel feeding points have also been linked to poor lateral dispersion of fuel in bubbling fluidised bed boilers with a large bed surface area (Niklasson et al., 2002.)

Another factor in the lateral mixing of fuel is how the fluidising air is fed into the bed. According to Scala et al. (2013, p. 106), the injection of air through relatively large nozzles at discrete locations may cause the fluidising gas to rise in distinct bubble columns, which leads to the formation of so-called mixing cells as can be seen in Figure 5. The effect of these mixing cells on the overall dispersion of fuel was studied by Olsson et al. (2012). They found that fuel particles spend most of their time in the areas between bubble columns. Additionally, it was found that the fluidisation velocity plays an important role in the lateral dispersion of fuel particles. This was attributed to increased interaction between bubbles, which would make bubble paths less consistent, and to the increased disturbances in the bed as larger bubbles pass through, resulting in stronger sinking of the dense emulsion. This can be seen in Figure 6, which shows the trajectory of a wood chip at two fluidisation velocities.

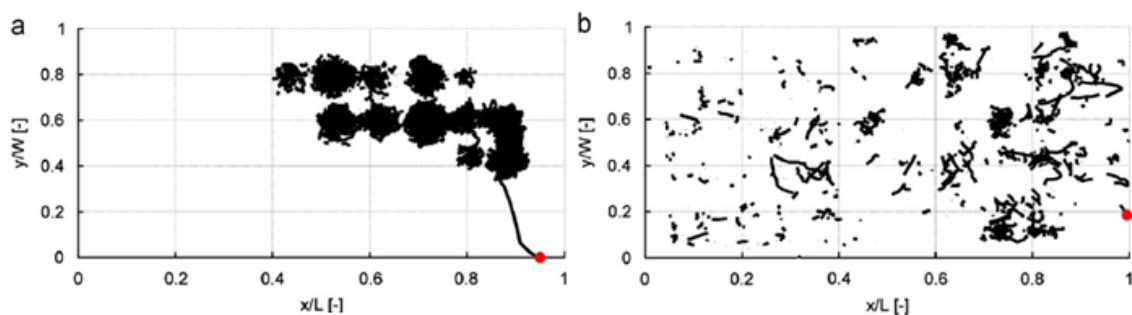


Figure 6. Trajectory of a wood chip on the bed surface at fluidisation velocities of (a) $u/u_{mf} = 5$ and (b) $u/u_{mf} = 7.5$, where u_{mf} is the minimum fluidisation velocity. The red dot marks the initial position of the particle, and discontinuities in the black line represent submersion of the particle in the bed. (Olsson et al. 2012.)

As can be seen, wood chips appear to stay very close to the bed surface. It was also reported by Scala (2013, pp. 331–332) that devolatilising fuel particles tend to be found near the surface of the bed, and that a significant portion of volatiles may be released above the bed surface, into the splashing zone.

Gas mixing in the splash zone is strongly linked to the bursting of bubbles on the bed surface. The drag of falling particles after a bubble bursts causes a downward flow in its central area. This results in two eddies being formed on either side of the collapsed bubble, which travel upwards with the gas flow. According to Vun et al. (2010), these vortices are the main source of turbulence above the bed surface, but this is likely only the case if air injection in the freeboard in the form of burners, air staging, and fuel feeding, which are common in industrial applications, is absent.

2.4.2 Freeboard mixing

After the splash zone, the remaining fuel must be oxygenated with secondary or tertiary air injected horizontally into the furnace. This is usually done in 2–4 levels to ensure proper mixing.

The secondary air nozzles may be arranged in several different ways. There may be nozzles in different numbers of walls, the nozzles may be of the same size or they may alternate between larger and smaller diameters, and in the case of rows of jets facing one another, these may have their centrelines aligned or staggered. (Holdeman et al., 2005.)

In the case of single-sided air feeding, all air in the injection level in question is fed through nozzles placed on one wall in the furnace. Mixing improves with traversed downstream distance x , or dimensionless distance x/H , H being the duct height or furnace depth. Optimal mixing happens when the momentum-flux ratios and nozzle spacing are such that the individual jets penetrate approximately halfway the depth of the furnace, i.e. the highest concentration of injected air is found in the middle of the channel after the flow has stabilised. (Holdeman et al., 2005.) The momentum-flux ratio J is defined as

$$J = \frac{u_j^2 \rho_j}{u_c^2 \rho_c} \quad (35)$$

where u_j and u_c are the inlet jet and cross-flow velocities
 ρ_j and ρ_c and the inlet jet and cross-flow densities.

The jet penetrating too deep into the furnace results in an imbalance between the inlet side and the opposing side of the stream due to most of the injected air flowing next to the opposing wall, whereas under-penetration results in the injected flow staying on the inlet side.

For opposed jets with centrelines in line, the optimal penetration depth is a quarter of the depth of the furnace since each side only needs to cover one half of the furnace depth. For staggered jets, the optimal penetration depth is three-quarters the furnace depth, as the opposing jets should bypass each other in an interlocking pattern, as illustrated in Figure 7. (Choi et al., 2016.)

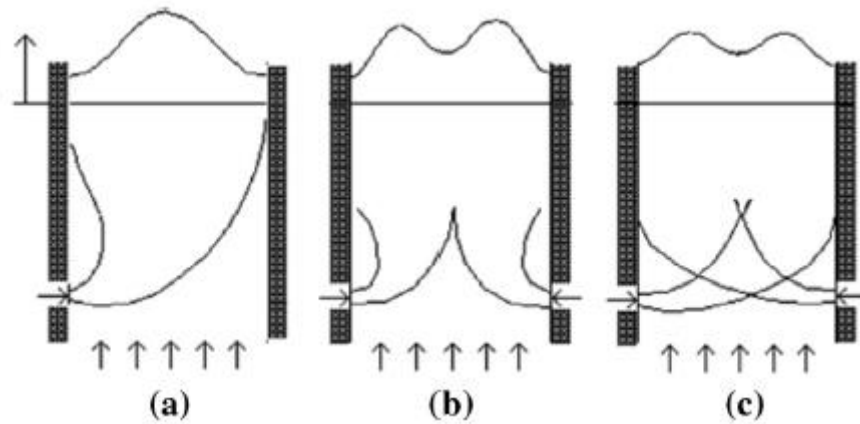


Figure 7. Ideal penetration and mixing for (a) single-sided injection, (b) double-sided in-line injection, and (c) double-sided staggered injection. (Choi et al. 2016)

Additionally, Holdeman et al. (2005) found that for a constant jet-to-crossflow mass-flow ratio, spacing the inlet nozzles too tightly results in the jets not penetrating deep enough, whereas spacing them too loosely results in overpenetration and weaker lateral mixing. They concluded that in the design of gas turbine engines, optimal mixing for single-sided injection could be reached when the mixing coefficient C had a value close to 2.5

$$C = S/H \sqrt{J} \quad (36)$$

where S is the spacing between adjacent nozzles

H is the duct height (equivalent to furnace depth)

In double-sided in-line injections, each side only needs to cover half the total area, and consequently the optimal value of C is 1.25, which translates to halved nozzle spacing and halved penetration depth. Similarly, the optimal value of C for staggered opposing jets was found to be 5, which is equivalent to transferring every other nozzle at optimal single-sided injection to the other side of the channel. (Holdeman et al. 2005.)

However, a recent study by Choi et al. (2016) has found that these predictions lose accuracy when used to calculate mixing in larger combustors, such as industrial sized incinerators that are closer in size to the furnaces modelled in this work. The main differences between gas engine air injection and larger industrial furnaces are longer

downstream distances in relation to inlet diameter (x/d) and significantly higher inlet velocities, and consequently momentum-flux ratios that can be dozens of times higher. The work of Holdeman et al. (2005) covered J values from 5 to 105, while the experiments done by Choi et al. (2016) were in the range of $J = 800$ – 1600 . According to Choi et al., this difference results in an increase in turbulent viscosity due to the higher kinetic energy of the secondary air injections, which causes the staggered jets to spread over a larger area and collide with the opposing jets instead of passing between them. The conclusion made was that for such applications, larger spacing between the jets is needed than predicted by the gas turbine engine model to ensure proper jet penetration, i.e. C should be significantly greater than 5. This is illustrated in Figure 8, where staggered jets of momentum-flux ratios of 1600 with a coefficient as high as $C = 8.0$ collide but increasing their spacing further allows the opposing jets to bypass one another and mix more efficiently.

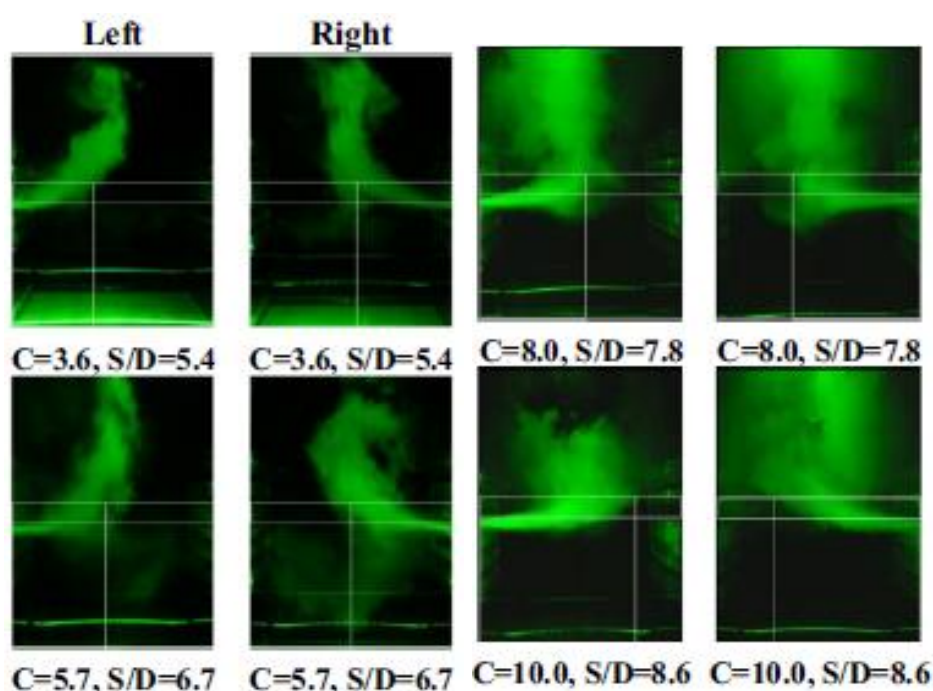


Figure 8. Gradually improving penetration with $C = 3.6$ – 10 for $J = 1600$. (Choi et al., 2016)

Another option is staggering the air inlets in such a way that every large nozzle faces a smaller nozzle on the opposite side, with nozzles on each side alternating between small and large. While this case was also modelled by Holdeman et al. (2010), the momentum-

flux ratio was roughly two orders of magnitude smaller than is common in large scale furnaces, and no other publicly available papers on this nozzle setup were found.

2.5 Existing models

Modelling of fluidised bed furnaces is a popular topic for research, with an abundance of different papers on the computational fluid dynamic modelling of these systems being available. In addition to these, some empirical models can be found. In this chapter, two models related to the current work will be reviewed, the first being created to model the mixing of air injections in a gas engine, and the second being built to model the operational conditions of fluidised bed boilers.

2.5.1 Mixing of a row of jets with a confined crossflow

In 2005, NASA published the MS Excel version of an empirical model created to calculate the mixing of gas jets in a crossflow. The geometry is illustrated in Figure 9.

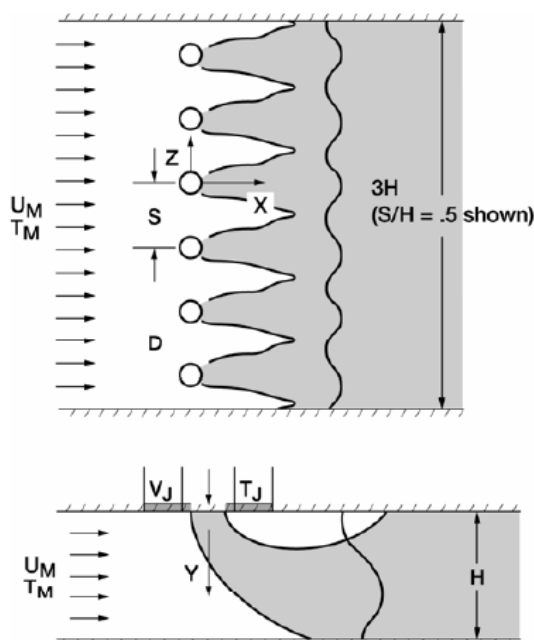


Figure 9. A row of jets mixing with a crossflow (Holdeman et al., 2005)

This model was developed to serve as a tool in the design of gas turbine engines, as there was a need to ensure efficient mixing between the injected air and the main gas flow to

create an even temperature profile at the exit of the combustor dilution zone, as quickly as possible, to minimise combustor length (Holdeman et al., 2005). While their model was designed and validated for significantly different conditions, namely lower duct heights and smaller momentum-flux ratios (Holdeman, 2016), this work should provide valuable insight into the most important variables in the modelling of mixing.

The approach of the model developed by NASA is based on the finding that conserved dimensionless scalar profiles in the axinormal plane can be expressed by (Holdeman et al. 2005):

$$\frac{\theta - \theta_{\min}^{\pm}}{\theta_c - \theta_{\min}^{\pm}} = \exp\left(\frac{-\ln(2)(y/H - y_c/H)^2}{(W_{1/2}^{\pm}/H)^2}\right) \quad (37)$$

The above equation uses six scaling parameters (θ_{\min}^+ , θ_{\min}^- , θ_c , y_c/H , $W_{1/2}^+$, and $W_{1/2}^-$) to calculate the shape of the scalar (θ) profile at any point in the flow field. θ_c is the maximum value of θ at a given x-coordinate, and θ_{\min}^{\pm} is its respective minimum value on the injection side (-) or on the opposite side (+). y/H is the dimensionless distance from the jet inlet wall, and y_c/H is the distance to the point with the highest value of θ , i.e. it describes the path of the main flow of θ as a function of axial distance. $W_{1/2}^{\pm}/H$ is the profile half-width value, i.e. the distance in the radial direction at which the profile drops from maximum to half-value. The minus and plus signs refer to the inlet or opposite side as with θ above. θ is the dimensionless scalar and is defined as

$$\theta = (T_c - T)/(T_c - T_j) \quad (38)$$

T is the local value of the conserved scalar (e.g. temperature or molar concentration in nonreacting flows), and T_c and T_j are the values for the cross-flow and jet flow, respectively. The scaling parameters and their definitions are shown in Figure 9.

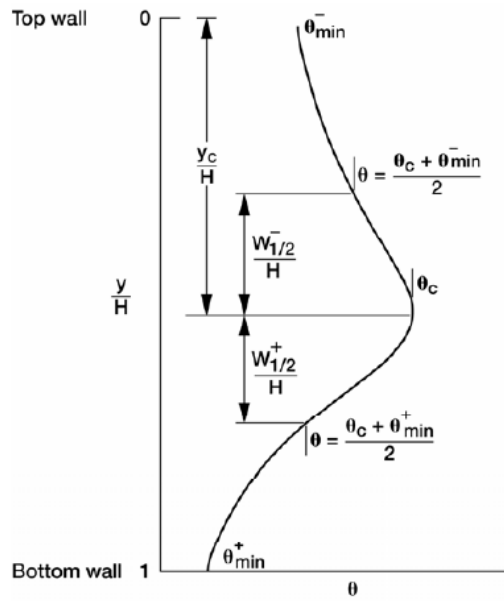


Figure 10. Scaling parameters (Holdeman et al., 2005)

The six scaling parameters are calculated using a number of empirical correlations, and thus the central profile can be obtained. Other correlations are used to calculate the scaling parameters needed to generate the remaining profiles, producing a discretised 2D profile of the flow cross-section at a given distance x . Multiple injection levels and opposed rows of jets are modelled by calculating the profiles of single rows of jets and superimposing them according to

$$\theta = \frac{[\theta_1 + \theta_2 - 2\theta_1\theta_2]}{[1 - \theta_1\theta_2]} \quad (39)$$

Where different θ s are the values obtained from different rows of jets.

One limitation in the model is that it should not be used if the calculated trajectory centre (y_c) is greater than the duct height (Holdeman et al., 2005). If the model were to be used outside its validity range, the modelled flow would not properly collide with the opposing wall, and the out-of-bounds scalar mass would simply be lost.

Additionally, the collision between two opposing jets is not modelled. While there is the possibility to calculate an effective duct height by assuming the collision between opposed jets is similar to that between a jet and a wall (Holdeman et al., 2005), this does

not seem to be the method used by the authors to model opposed jets of different sizes. Instead, the superimposition model was used, but the modelled downstream distance was limited to the point where the opposing jets would collide. It appears that should the downstream distance be increased beyond that, the jets would pass each other without interaction, akin to waves. If the effective duct height approach was used, the problem would be the loss of scalar mass past the effective duct height due to truncation.

Overall, their model was made for a significantly different application, and its implementation in the current work does not seem feasible. The NASA model was developed for applications of roughly $J < 100$, while the furnaces modelled in this work can have momentum-flux ratios in the order of thousands. Additionally, due to how quickly the inlet jets reach the opposing walls, the jet centreline trajectory would leave the furnace boundaries within a short downstream distance, after which a large share of the conserved scalar mass would be lost.

2.5.2 Comprehensive simulation program for fluidised beds

Submitted as a doctorate thesis by M. L. de Souza-Santos (1987), the comprehensive simulation program for fluidised bed equipment (CSFB) model was developed to simulate a wide range of steady-state operating conditions in fluidised bed combustion and gasification plants. Modelled aspects include the bubble and emulsion composition profiles in the bed area, gas phase composition profile along the freeboard height, temperature profiles of all phases for the entire furnace height, solid particle size distributions throughout the furnace, heat transferred to walls, and pressure losses in the gas phase. For the particle size distribution, the effects of elutriation, entrainment, attrition and recycling are considered. The main relations between the different elements of the bubbling fluidised bed model are illustrated in Figure 11.

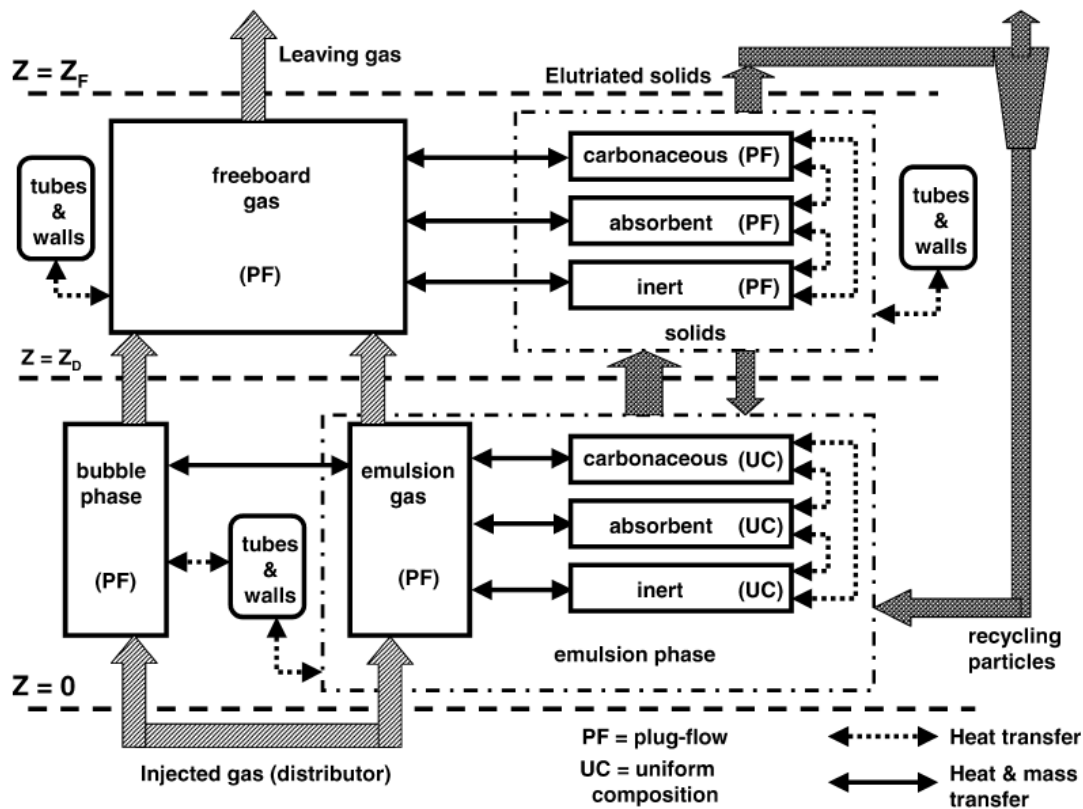


Figure 11. Diagram depicting main relations and assumptions in the model (de Souza-Santos, 2007)

The model is one dimensional, and the furnace area is split in two regions, the bed and the freeboard. The bed volume is occupied by two main phases, the solids-free bubble phase and the emulsion phase, both of which are assumed to move upwards in an inviscid plug flow. The form, velocity, and dimensions of the bubbles are calculated as a function of bed height, and they exchange mass and heat with the gaseous and solid parts of the emulsion phase. The solids main phase consists of three sub-phases: fuel, inert and sulphur absorbent. The solids composition in the bed area is assumed to be uniform, but the temperature profile is one dimensional and calculated based on energy balances. These include heat exchange between the different solid and gaseous species, as well as surface elements and heat generated via chemical reactions. (de Souza-Santos, 2007.)

The freeboard consists of gaseous and particulate phases, which again are assumed to be in an inviscid plug flow. Entrainment, elutriation, and disengagement of particles are modelled for the most part according to the method described in chapter 2.1.3. Chemical

reactions continue to happen in the freeboard, as does heat and mass transfer. The gases are assumed to be transparent to radiation throughout the furnace volume, and radiation is modelled between particles and surfaces. An update to the radiation sub model in the bed area was later published (Rabi & de Souza-Santos, 2003), but produced no significantly different results.

The model was tested against two pilot-scale furnaces, of which the larger one was owned by Babcock and Wilcox. This unit has a $0.9 \times 0.9 \text{ m}^2$ cross-section area, with the 3.4 m high vertical walls fully covered by refractory. The fuel used was subbituminous coal, fed at a rate of 58.5 g/s. The entire air flow (695 g/s) was fed through the grid. The calculated temperature profiles of the different phases are shown below in Figure 12. (de Souza-Santos, 2007.)

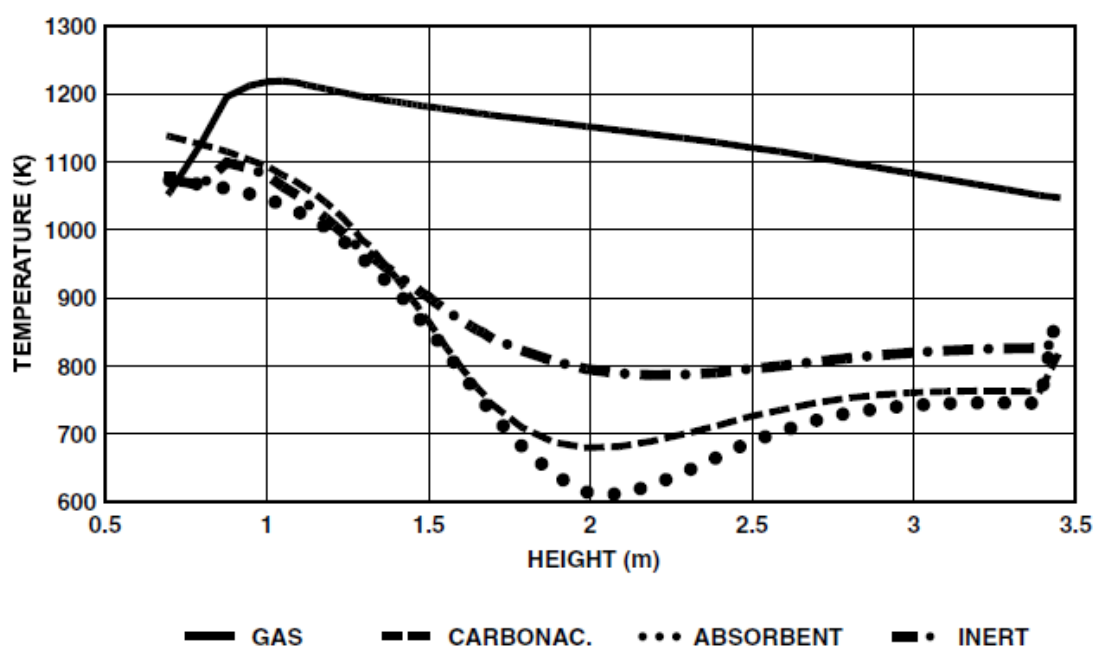


Figure 12. Simulated temperature profiles of different phases in the freeboard of the B&W test unit. (de Souza-Santos, 2007.)

The difference between simulated and measured temperatures was in the order of 20-30 °C at the distributor, the middle of the bed, and at the top of the freeboard, while at the bed top (height = 0.7 m) the model overpredicted the temperature by approximately 100 °C. The full results can be found at de Souza-Santos (2007).

3 THE BFB FURNACE MODEL

The BFB furnace model is a 1D model created with the goal of providing fast and relatively accurate information on furnace conditions. Since it deals with many insufficiently understood phenomena in an incomplete 1D geometry, it uses empirically derived correlations to produce results in line with measurements instead of attempting to physically model these phenomena. This chapter provides an overview of the model and describes some of its key components.

3.1 Principles

The model uses information regarding the furnace geometry, fuel composition, and air injections to produce an estimate of the temperature and heat transfer profiles in the furnace. These are summarised in Figure 13.

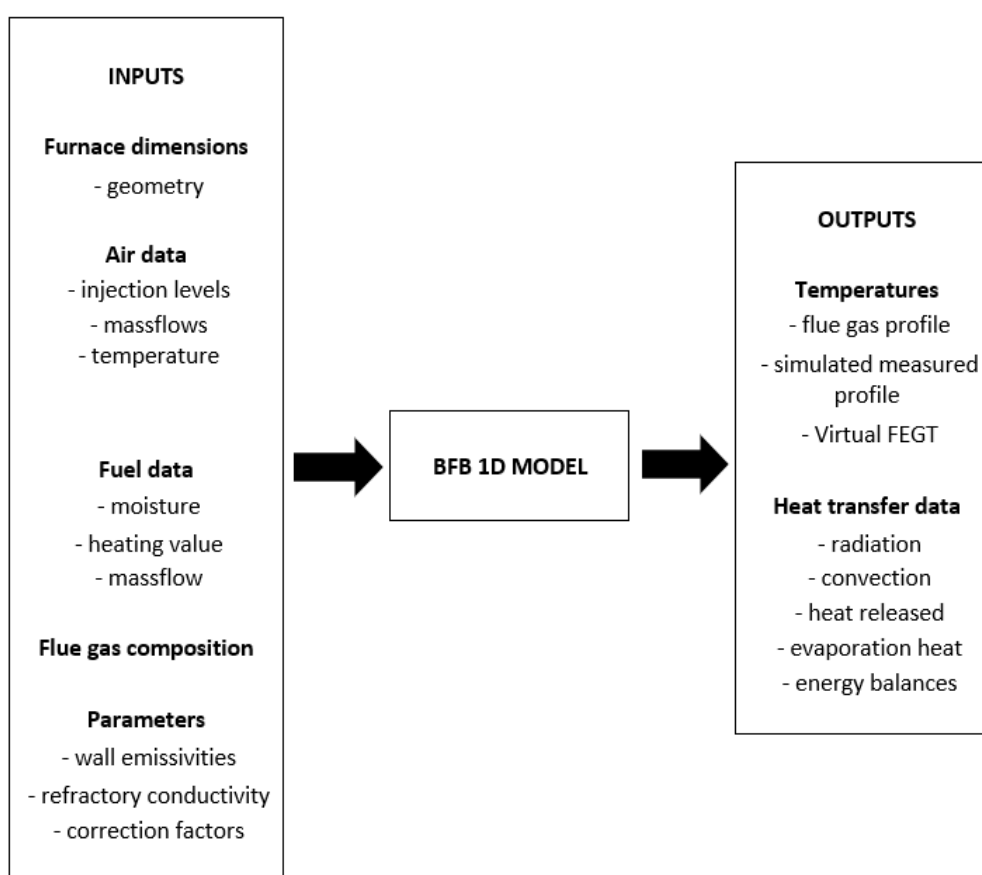


Figure 13. Main inputs and outputs of the model

In practice, the boiler dimensioning program of Sumitomo SHI FW is used to calculate most of the inputs needed for this model, such as ash, flue gas composition, and stoichiometric combustion air data, which are based on the fuel composition and mass flow. Similarly, the furnace exit gas temperature (FEGT) is selected to satisfy the heat balance of the heat transfer surfaces in the back-pass.

At first, the furnace area is divided vertically into a number of volume elements. The refractory covered area is split into three blocks, with the bed occupying the lowest volume, and the remaining furnace is divided into equally sized elements depending on the number of elements wanted, as illustrated in Figure 14. Typically, the total number of elements varies between 6 and 16.

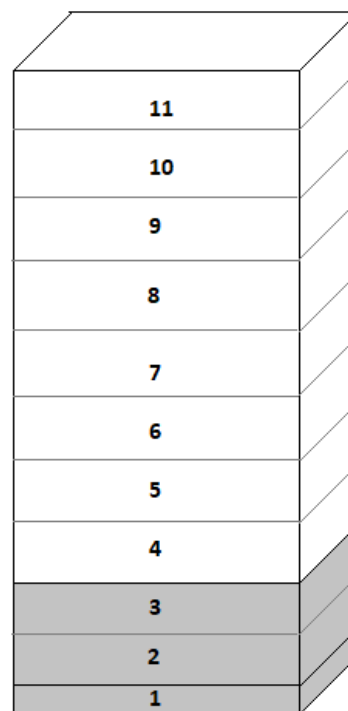


Figure 14. Division of the furnace geometry into calculation blocks, where element 1 represents the bed, and the grey area occupied by elements 1–3 represents the refractory lined area.

With the fuel and air mass flows known, the heat release profile in the furnace can be calculated, and the mass balances and energy balances of the calculation blocks can be written. Finally, the temperature profile is solved iteratively along with heat transfer. If a target FEGT has been selected for the furnace, the energy balances are solved again with

an adjusted radiation correction factor until the desired FEGT has been reached. The calculation process is illustrated in Figure 15.

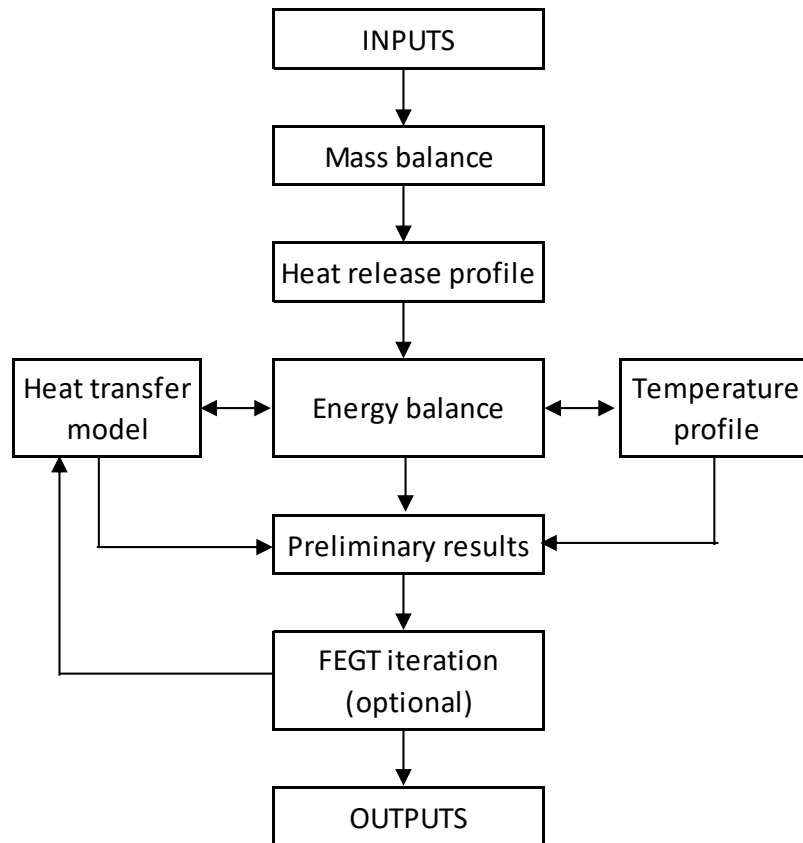


Figure 15. Calculation procedure of the 1D BFB model

3.2 Heat and mass balances

The two keystones of a physical model are the laws of conservation of mass and energy. The conservation of momentum is used in fluid dynamic models, but its implementation in a one-dimensional furnace model is not feasible. In the model presented in this work, the mass balance of volume element i is given by

$$q_{m,\text{fuel}} + q_{m,\text{fg in}} + q_{m,\text{air}} + q_{m,\text{rg}} = q_{m,\text{fg out}} \quad (40)$$

where

- $q_{m,\text{fg in}}$ is the mass flow of flue gases entering the element
- $q_{m,\text{fuel}}$ is the mass flow of fuel being fed into the element
- $q_{m,\text{air}}$ is the mass flow of air being fed into the element

$q_{m,rg}$ is the mass flow of recirculation gas entering the element
 $q_{m,fg\ out}$ is the mass flow of flue gases exiting the element

As can be seen, no mass balances are used for different species. Only the preservation of overall mass is considered, and the flue gases are assumed to have the same composition throughout the furnace volume. This composition is that of the furnace exit, obtained with the assumption of ideal combustion.

The energy balance of a volume element is given by

$$Q_{fg,in} + Q_{air,in} + Q_{rg,in} + Q_{fuel,sens} + Q_{comb} = Q_{fg,out} + Q_{losses} + Q_{ht} \quad (41)$$

where

- $Q_{fg,in}$ is the convection heat of flue gases entering the element
- $Q_{air,in}$ is the sensible heat of air injected in the element
- $Q_{rg,in}$ is the sensible heat of recirculation gas fed into the element
- $Q_{fuel,sens}$ is the sensible heat of fuel fed into the element
- Q_{comb} is the heat released by combustion reactions in the element
- $Q_{fg,out}$ is the outgoing convection heat of flue gases from the element
- Q_{losses} is the sum of heat losses in the element, such as moisture evaporation or calcination reactions
- Q_{ht} is the net heat leaving the element due to heat transfer

The net heat transfer power Q_{ht} can be either negative or positive and includes convection to walls and radiation to and from all other elements.

3.3 Entrainment

It is possible to model the effect of fuel entrainment by giving the share of entrained fuel as an input. Entrained fuel is assumed to never enter the bed area, and this is reflected in the heat release, moisture evaporation, and mass balance of the bed and of the entire furnace.

The possibility to estimate the share of entrained fuel in the model itself was also considered but not implemented due to its complexity and high inaccuracy expected. The

estimation of entrainment by calculating the terminal velocity for parcels of particles of a given shape and size would be problematic due to the highly varied shapes and densities of the fuel used alone. Additionally, the change in particle density and size as it undergoes the processes of drying, devolatilisation, and attrition would introduce new uncertainties, and the heterogeneous flow structures present in the bed and freeboard of the furnace mean that the terminal velocity of individual particles cannot be directly compared to the average flow velocity of the flue gases to determine whether they become entrained or not. Furthermore, due to the conversion times of char particles being roughly proportional to the square of their diameter, small errors in the particle size of entrained fuel would result in significant error in the estimated amount of unburned char leaving the furnace.

Another option would be to use the methods presented in chapter 2.1.3 to estimate the entrainment of solid particles, but the existing correlations produce highly varied results, and validation of any entrainment model would be challenging due to the difficulty in measuring it in commercial scale furnaces.

3.4 Gas absorption coefficient

The absorption coefficient of a gas describes how efficiently it absorbs and emits radiation and is a key parameter in the modelling of radiative heat transfer in a furnace. In the model, the gas absorption coefficient accounts for the effect of both gases and particles on the radiative properties of the gas-solids suspension. The absorption coefficient depends on the gas temperature, composition, dust content, and dust properties, and is estimated by the model by assuming that it would be proportional to the flue gas density. The gas absorptivity correlation was modified in the course of the current work and is described in more detail in chapter 4.5.

3.5 Heat release

The accurate estimation of the heat released in different parts of the furnace was of high priority in this work. This is due to the high amount of energy stored in the fuel, and consequently, its high impact on the temperature profile generated. However, the heat release in a furnace is a complex phenomenon, heavily influenced by three-dimensional

flow structures and local concentrations of oxygen and combustible species, and it was clear from the beginning that severe simplifications would have to be made if this was to be calculated in a 1D model.

The first simplification was not to implement combustion equations at all. This was done because the combustion of gases in the freeboard is mainly dependent of their mixing with oxygen (Scala et al., 2013, p. 335). Additionally, from a computational perspective, the use of kinetic reaction rates, which are temperature-dependent, would add an extra iterative loop in the program, increasing computational time as well as being a possible issue when it comes to stability, since an increase in temperature would further increase heat release, which would in turn result in a higher temperature, and so forth. Instead, the fuel composition and mass flow are used to calculate the stoichiometric air flow $q_{m,st,tot}$ needed to fully oxidise the fuel, and this stoichiometric air mass flow represents the fuel in the calculations. Thus, the way the fuel is used in calculations can be seen as a mirror image of the stoichiometric air needed to oxygenate it. This being established, the maximum heat release $Q_{max,i}$ in element i is given by

$$Q_{max,i} = Q_{fuel} X_{max,i} \quad (42)$$

where Q_{fuel} is the total fuel heating power, given by the product of fuel mass flow and fuel lower heating value (LHV)

and $X_{max,i}$ is the maximum heat release coefficient, defined as

$$X_{max,i} = \frac{\min(q_{m,air,i}; q_{m,st,i})}{q_{m,st,tot}} \quad (43)$$

where $q_{m,air,i}$ is the air mass flow in element i

$q_{m,st,i}$ is the stoichiometric air flow needed to oxygenate the fuel in element i

$q_{m,st,tot}$ is the stoichiometric air flow needed to oxygenate all the fuel fed into the furnace

The actual heat release in element i X_i is obtained by multiplying the maximum possible heat release by the coefficient f_i as given below

$$X_i = X_{max,i} f_i \quad (44)$$

f_i is an empirical coefficient that is used to estimate how much of the maximum available heat release happens in a given element. The maximum heat release can be reduced by insufficient residence time or imperfect mixing, for example. The calculation of the heat release parameter f_i in the freeboard will be presented in more detail in chapter 4.4, and for the bed area, the correlation used is a function of the share of grid air, as given by

$$f_{\text{bed}} = a \ln(q_{\text{m,air,bed}}/q_{\text{m,air,tot}}) + b \quad (45)$$

where

| | |
|------------------------|--|
| a | is an empirical parameter |
| b | is an empirical parameter |
| $q_{\text{m,air,bed}}$ | is the air grid air flow |
| $q_{\text{m,air,tot}}$ | is the total air flow into the furnace |

3.6 Moisture evaporation

Evaporation of fuel moisture is a significant heat sink and has a strong impact on the temperature profile of the lower furnace area. It is known that fuel drying happens shortly after it is fed into the furnace but estimating the drying rate quantitatively as a function of furnace height is not straightforward.

To begin with, measurements on fuel drying in a furnace are difficult to make, with the measured temperature profile giving indirect information on the net heat balance as a function of height. The problem here is that even if the net heat transfer in the form of convection and radiation is assumed to be known, the heat release and moisture evaporation are both being fit to the measured temperature profile, with no accurate way of differentiating between them. This is not accounting for possible measurement errors due to radiation to walls, or due to measuring a non-representative three-dimensional flow structure such as an air inlet or a hot flue gas channel in the middle of the furnace cross-section. The remaining option is to attempt to qualitatively assess the evaporation rate at different points in the furnace, and this was the approach used.

The fuel is fed in the furnace from chutes in the surrounding walls, with primary air being blown through the chutes in order to spread the fuel over a large area. Assessing how well the fuel feeding system succeeds in spreading the fuel is the first difficulty. A

homogeneously spread fuel would be in contact with hot main flow, resulting in higher heating rates and faster drying as it falls. On the other hand, the fuel failing to spread would result in a strongly stratified flow, with poor mixing and little drying before the fuel reaches the bed.

Even after reaching the bed, fuel particles may be flung into the splash zone by bubble eruptions, and this may result in some more drying happening outside the bed area, however this was assumed to be of little impact. Thus, it was assumed that all moisture evaporation happening outside the bed area happens as the fuel is falling. While this has no effect on the heat balance of the furnace, it does affect the mass balance of the bed, which has an effect on the bed temperature.

The moisture evaporation heat of element i was modelled according to

$$Q_{\text{H}_2\text{O},i} = q_{\text{m,H}_2\text{O}} l_{\text{H}_2\text{O}} x_{\text{H}_2\text{O},i} \quad (46)$$

where $q_{\text{m,H}_2\text{O}}$ is the fuel moisture mass flow
 $l_{\text{H}_2\text{O}}$ is the latent heat of water evaporation at $T = 25 \text{ }^\circ\text{C}$
 $x_{\text{H}_2\text{O},i}$ is the share of evaporation happening in element i

The share of evaporation in the bed area was estimated to be 60 %, with the remainder being split between the next two elements as a function of their height. Half of the entrained fuel moisture was assumed to evaporate in the second, and the other half in the third element. This is a very simple division, and it could be modelled more elaborately if time was not a constraint but modelling the temperature of the region above the bed is not a high priority in this work as the temperature profile is mainly used to determine the ammonia feeding level in the furnace, which happens at higher elevations.

3.7 Convection

Gas convection into the furnace walls of element i is calculated according to

$$Q_{\text{conv},i} = \alpha_i A_{\text{w},i} (T_{\text{G},i} - T_{\text{w},i}) \quad (47)$$

where T_{G} is the gas temperature
 T_{W} is the tube wall temperature

A_w is the vertical wall area around the gas element
 α is the heat transfer coefficient

In the freeboard, the temperature difference between the tube wall surface and the drum is kept constant, as the low conductivity of steel combined with the efficient heat transfer between the tubes and water would prevent the wall surface temperature from increasing too much. In the refractory lined area, this temperature difference between the drum and the steel wall surface is smaller due to weaker heat transfer through the refractory. The refractory surface temperature can then be calculated by the model by using refractory thickness and conductivity data combined with the radiative and convective heat fluxes obtained by heat transfer calculations.

The convective heat transfer coefficient is estimated by

$$\alpha_{\text{conv},i} = B u_{G,i} + C \quad (48)$$

where $u_{G,i}$ is the average flow gas velocity in element i
 B is an empirical parameter
 C is an empirical parameter.

In the bare-tube freeboard, this is the heat transfer coefficient used. In the lower furnace, the insulating effect of the refractory is considered, yielding

$$\alpha_i = \left(\frac{1}{\alpha_{\text{conv},i}} + \frac{s_{\text{ref}}}{k_{\text{ref}}} \right)^{-1} \quad (49)$$

where s_{ref} is the refractory thickness
 k_{ref} is the thermal conductivity of the refractory

In the bed area, the convective heat transfer coefficient is estimated to have a constant value of 500 W/m²K.

3.8 Radiation

Modelling of radiative heat transfer in the furnace was done using the zone method by Siegel and Howel, in which the furnace freeboard is assumed to be divided into N isothermal zones. The furnace is thought to consist of a grey medium with a constant

absorption coefficient capable of emitting and absorbing, but not of scattering radiation. This medium is enclosed by grey, diffuse surfaces capable of emitting, absorbing and reflecting radiation. (Modest 2013, p. 590).

The total number of elements in the system is then equal to N volume elements, each surrounded by four walls. The bed surface and the furnace exit are modelled as surface elements. By simplifying the furnace geometry as a square cross-section, the four surrounding walls can be combined into a single surface element, bringing the total number of surfaces to $N + 2$. All elements radiate to all other elements, as shown in Figure 16, and the radiative power between elements is calculated using direct exchange areas.

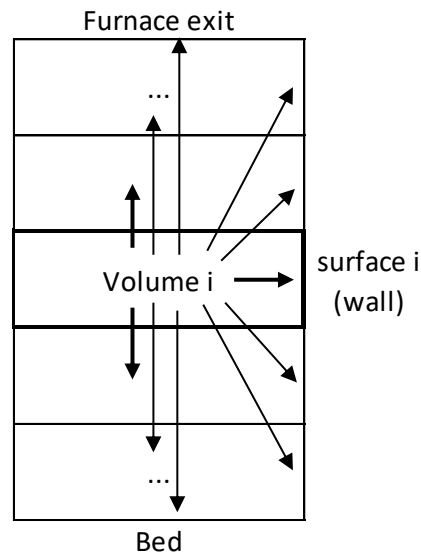


Figure 16. Emission of radiation from a volume element i to all other volume and surface elements in the furnace.

The direct exchange area between two surfaces is defined as

$$\overline{s_i s_j} = \overline{s_j s_i} = \frac{Q_{i \rightarrow j}}{J_i} \quad (50)$$

where $Q_{i \rightarrow j}$ is the total direct heat flux from zone i reaching zone j
 J_i is the radiosity of zone i

According to Modest (2013, p. 590), for the infinitesimally small surface areas dA_i and dA_j shown in Figure 17a, the heat flux leaving i and reaching j is given by

$$Q_{i \rightarrow j} = \left(\frac{J_1}{\pi} \right) (dA_i \cos \theta_i) \frac{dA_j \cos \theta_j}{S^2} e^{-as} \quad (51)$$

where the first term is the intensity leaving dA_i in the direction of dA_j . The second term reduces the radiation intensity according to the angle between the ray and the surface normal. The third term is the solid angle subtended by dA_j , and the last term accounts for the radiation intensity reduction caused by the absorbing media between the two surfaces, a being the gas absorptivity coefficient and S being the traversed distance.

The surface-to-surface direct exchange area can be found by inserting equation 51 in equation 50 and integrating over dA_i and dA_j

$$\overline{s_i s_j} = \int_{A_i} \int_{A_j} e^{-as} \frac{\cos \theta_i \cos \theta_j}{\pi S^2} dA_j dA_i \quad (52)$$

Similarly, the heat flux emitted from volume i to surface j is given by

$$Q_{i \rightarrow j} = (4aE_{bi}dV_i) \frac{dA_j \cos \theta_j}{4\pi S^2} e^{-as} \quad (53)$$

where the first term is the energy emitted from a volume of gas to all 4π directions, the second term gives the fraction of the solid angle subtended by dA_j , and the last term accounts for the attenuating effect of the absorbing medium. The emissive power E_{bi} is used here instead of J , as the radiation reflected by the gas is not considered.

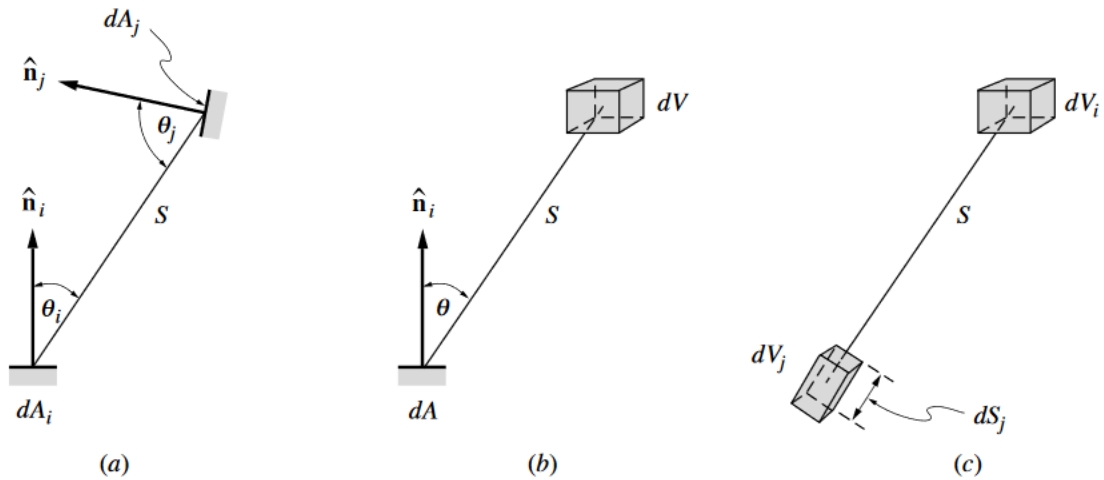


Figure 17. Radiative exchange between the different elements modelled: (a) two surfaces, (b) surface and volume, (c) two volume elements (Modest 2013, p. 591)

The volume-to-surface direct exchange area can then be calculated according to

$$\overline{g_i s_j} = \overline{s_j g_i} = \int_{V_i} \int_{A_j} e^{-as} \frac{\cos \theta_j}{\pi S^2} a dA_j dV_i \quad (54)$$

By orienting the receiving gas volume j with the surface area dA_j perpendicular to radiation as shown in Figure 17c, the heat flux emitted from volume i absorbed by volume j is given by

$$Q_{i \rightarrow j} = (4aE_{bi}dV_i) \frac{dA_j}{4\pi S^2} e^{-as} a dS_j \quad (55)$$

where dS_j is the ray path length through gas volume j

The first three terms are as for volume-to-surface radiation, with the fourth term taking into account the partial transparency of the receiving gas. This leads to a volume-to-volume direct exchange area of

$$\overline{g_i g_j} = \int_{V_i} \int_{V_j} e^{-as} \frac{a^2}{\pi S^2} dV_j dV_i \quad (56)$$

These direct exchange areas are calculated by dividing the zone volumes and surfaces into smaller elements and performing numerical integration over them. Once these exchange areas have been calculated, they are smoothed to ensure that the sum of all individual radiation fluxes of an element correspond to its total radiative heat flux. The radiative heat flux from gas element i to element j can then be calculated as

$$q''_{i \rightarrow j} V_j = \overline{g_i g_j} \sigma T_i^4 \quad (57)$$

where T_i is the temperature of the emitting element in K

Similarly, for gas-surface radiation

$$q''_{i \rightarrow j} A_j = \overline{g_i s_j} \sigma T_i^4 \quad (58)$$

For surface-surface radiation, the reflected radiation is included in the radiosity as

$$q''_{i \rightarrow j} A_j = \overline{s_i s_j} J_i = \overline{s_i s_j} (\varepsilon_i \sigma T_i^4 + (1 - \varepsilon_i) \sum q''_{i, \text{in}}) \quad (59)$$

where $q''_{i, \text{in}}$ are radiative fluxes that reach surface i

Once the emitted radiation of each element is known, their net radiation can be calculated, and the temperatures obtained by solving the overall energy balance.

4 MODEL DEVELOPMENT

In this chapter, the most significant changes made to the model will be presented. The main objective was to improve the accuracy of the temperature profile generated, and special emphasis was placed on the heat release profile, due to the large amount of energy released via combustion.

4.1 Thermocouple measurement error

Before attempting to match the temperature profile generated by the model to the measured profiles of various plants, the measurement error of the thermocouple was estimated. If the thermocouple was shielded from radiation, or if it was surrounded by an optically thick gas, it would be in thermal balance with the surrounding gas. However, a thermocouple in a furnace receives and emits radiation to all other visible elements, as shown in Figure 18. These elements can be walls, hot gas volumes in other parts of the furnace, and the bed surface. Because of this, its temperature may differ from the gas temperature it is currently measuring.

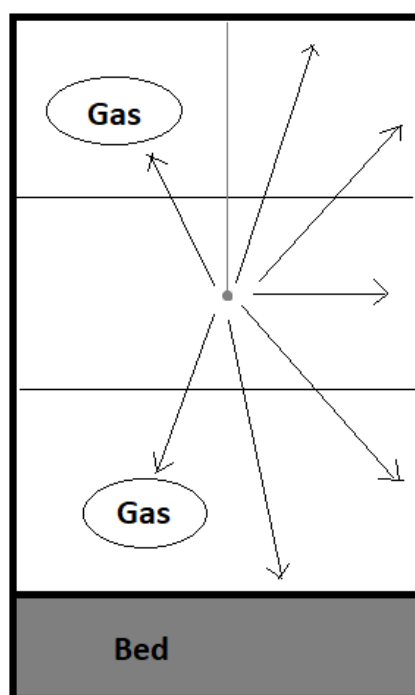


Figure 18. Radiation net of a thermocouple in a furnace

The energy balance of a thermocouple in thermal equilibrium may be written as

$$q''_{\text{conv}} = q''_{\text{r,w}} + q''_{\text{r,bed}} + \sum_j^N q''_{\text{r,g,j}} \quad (60)$$

where q''_{conv} is the convective heat flux to the surrounding gas
 $q''_{\text{r,w}}$ is the radiative net heat flux to the walls
 $q''_{\text{r,bed}}$ is the radiative net heat flux to the bed surface
 $\sum_j^N q''_{\text{r,g,j}}$ is the radiative net heat flux to all gas elements

The convective heat flux is given by

$$q''_{\text{conv}} = h(T_g - T_{\text{tc}}) \quad (61)$$

where T_g is the surrounding gas temperature
 T_{tc} is the temperature of the thermocouple
 h is the convective heat transfer coefficient, solved from the Whitaker correlation given below

$$\text{Nu}_D = \frac{hD}{k} = 2 + (0.4 \text{Re}_D^{0.5} + 0.06 \text{Re}_D^{0.67}) \text{Pr}^{0.4} \quad (62)$$

where Nu is the Nusselt number
 D is the thermocouple diameter
 k is the thermal conductivity of the gas
 Re_D is the Reynolds number of the flow around the thermocouple, using its diameter as the characteristic length
 Pr is the Prandtl number of the gas

The radiative heat fluxes were calculated by calculating the view factors between it and the other elements in the furnace as explained in chapter 3.8.

Now, the corrected gas temperature of the measured profiles could be calculated, or the model could be updated to simulate what the measured temperature profile of the modelled furnace would be. The latter option was chosen, and the thermocouple temperature could then be solved by combining equations 60 and 61 as below

$$T_{\text{tc}} = T_g - (q''_{\text{r,w}} + q''_{\text{r,bed}} + \sum_j^N q''_{\text{r,g,j}})/h \quad (63)$$

4.2 Afterburning

Often the furnace exit gas temperature (FEGT) measured was lower than the FEGT required to fulfil the energy balance of the boiler. In some occasions, this difference was very significant. This was attributed to afterburning, i.e. heat release outside the furnace model boundary due to incomplete burning of fuel in the furnace area, as illustrated in Figure 19.

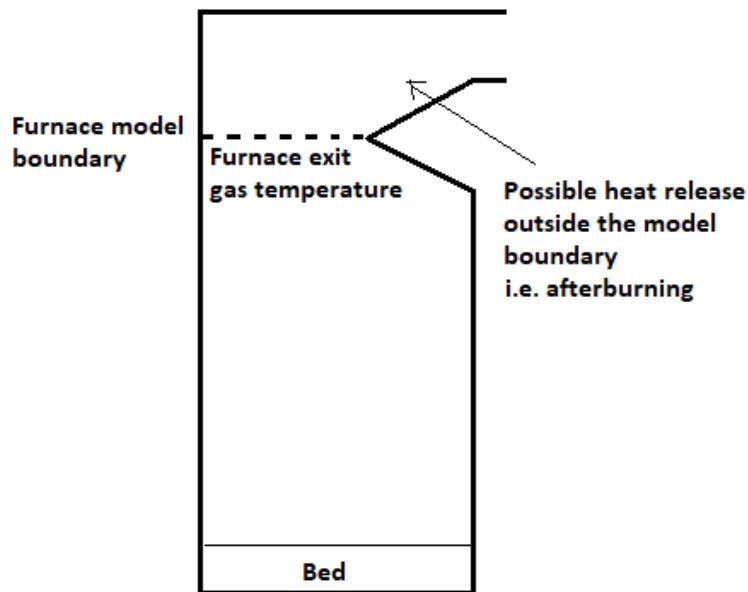


Figure 19. Heat released outside the model boundary would result in the furnace exit gas temperature (FEGT) being lower than predicted if all fuel was assumed to burn within the boundary.

4.2.1 Implementation as user input

The modelling of afterburning was implemented by adding a post-combustion factor f_{pc} , which is the ratio of heat being released outside the model boundary to the total fuel heating power. The factor f_{pc} was a user input at this point, as the amount of afterburning happening was unknown. The remaining heat was then assumed to fully burn in an additional element just after the furnace boundary as given by

$$Q_{pc} = f_{pc} Q_{fuel} \quad (64)$$

where Q_{pc} is the heat released in the additional element
 Q_{fuel} is the total fuel heating power

No heat transfer was modelled in this additional element, as the heat transfer of superheaters is not part of the current model, and the main objective was to satisfy the boiler energy balance while attempting to follow the measured temperature profile. A second FEGT is calculated for this additional element, with the purpose of checking whether the solution obtained satisfies the boiler energy balance. This energy balance FEGT, or $T_{FEGT,eb}$ is calculated according to

$$T_{FEGT,eb} = T_{FEGT} + \frac{Q_{pc}}{q_{m,fg} \cdot c_{p,fg}} \quad (65)$$

where T_{FEGT} is the modelled gas temperature as it leaves the furnace area
 $q_{m,fg}$ is the flue gas mass flow leaving the furnace
 $c_{p,fg}$ is the flue gas specific heat capacity

4.2.2 Cases used in validation

With the simple afterburning submodel implemented, the amount of afterburning happening in different plants was estimated. This was done by back-calculating a number of cases and matching the FEGT required by the boiler energy balance to the energy balance FEGT calculated above, and the measured FEGT to the FEGT obtained by simulating a thermocouple measurement at the furnace exit, as presented in chapter 4.1.

A back-calculation is the modelling of an existing plant. By using measured fuel and air data to calculate the boiler operating parameters and temperatures, these can be compared to measurements as a way of checking how well the design calculations match reality.

A total of 16 cases were calculated in total, and these are shown in Table 2 below. These same cases were used to validate the rest of the model as well.

Table 2. Cases re-calculated to validate the model. ⁽¹⁾ FR = Forest residue.

| Case | Load [%] | Fuel |
|-------------|----------|-------------------------------|
| Boiler A, 1 | 100 | Bagasse |
| Boiler A, 2 | 100 | Bagasse |
| Boiler B, 1 | 95 | Chips, FR ⁽¹⁾ |
| Boiler B, 2 | 52 | Chips, FR ⁽¹⁾ |
| Boiler B, 3 | 94 | Peat |
| Boiler B, 4 | 47 | Peat |
| Boiler B, 5 | 100 | Chips, FR ⁽¹⁾ |
| Boiler C, 1 | 100 | Bio mix |
| Boiler C, 2 | 100 | Bio mix |
| Boiler C, 3 | 25 | Bio mix |
| Boiler C, 4 | 50 | Bio mix |
| Boiler D | 70 | Peat, bark, FR ⁽¹⁾ |
| Boiler E | 100 | FR ⁽¹⁾ |
| Boiler F | 100 | Bark, paper |
| Boiler G, 1 | 94 | Sludge mix |
| Boiler G, 2 | 52 | Sludge mix |

4.2.3 Estimation of afterburning

The fitting was done by changing the radiation correction factor and the post-combustion factor. The radiation correction factor had to be increased to ensure that the same heat is transferred to the furnace walls despite the furnace temperature being lower due to the reduced heat release. This gives an estimated amount of afterburning for each of the cases calculated, which were then used to find a correlation capable of predicting the share of fuel energy not released in the furnace area. The estimated afterburning shares are shown below in Figure 20. The correlation used is

$$f_{pc} = a - (b \lambda + c h_{furn}) \quad (66)$$

where

| | |
|------------|-----------------------------------|
| a | is an empirical parameter |
| b | is an empirical parameter |
| c | is an empirical parameter |
| λ | is the combustion air coefficient |
| h_{furn} | is the furnace height |

Naturally, f_{pc} is limited to values between 0 and 1. Boiler D was not included in the correlation fitting as it is clearly an outlier. This is thought to be caused by the depth of the highest measurement point being only 1.6 m, while the remaining points were measured in depths of 3.5–3.9 m. This is likely to cause a significantly higher measurement error due to radiation than predicted, as the model estimates the error using a constant distance to the wall. Since the afterburning share was estimated based on the difference between measured FEGT and that required by the boiler heat balance, the measured temperature being much lower than reality would result in a severe overestimation of afterburning.

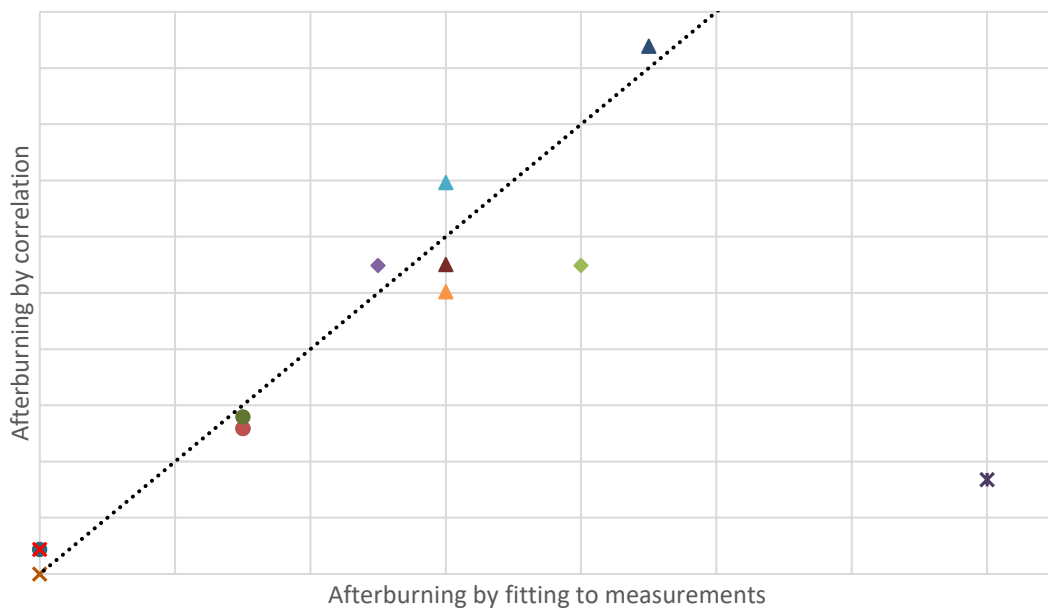


Figure 20. Afterburning shares matched to measurements vs estimated by correlation

It can be seen that there are deviations between matched and calculated values, combined with a relatively low number of data points. Additionally, the correlation is clearly too simple to be able to accurately evaluate what in reality is a complex function of fuel properties and three-dimensional gas flows, dependent on nozzle arrangement, air injection conditions, fuel entrainment and chemical reactions. Afterburning could also be estimated by allowing the heat release model to produce an incomplete profile, i.e. a profile where not all fuel is forced to burn in the furnace area. However, that would likely require a more refined model, where the air injection system is modelled in more detail

and where the furnace is modelled in a higher number of dimensions, since the main reasons for incomplete combustion are thought to be stratified flows of oxygen and combustible gases, along with insufficient residence time of entrained char particles.

4.3 Splitting of secondary air injection

When the 1D BFB model was originally built, the volume elements were divided according to the secondary air inlet levels, so that every inlet was always at the bottom of a relatively large element. As such, the injected air had enough time to mix with the flue gases, and the assumption of isothermal and well-mixed elements was acceptable. However, in subsequent updates to the model made some years ago, the furnace division method was changed to calculate the element dimensions based on the wanted number of elements, resulting in equally sized blocks that are independent of air injection levels, as shown in Figure 21.

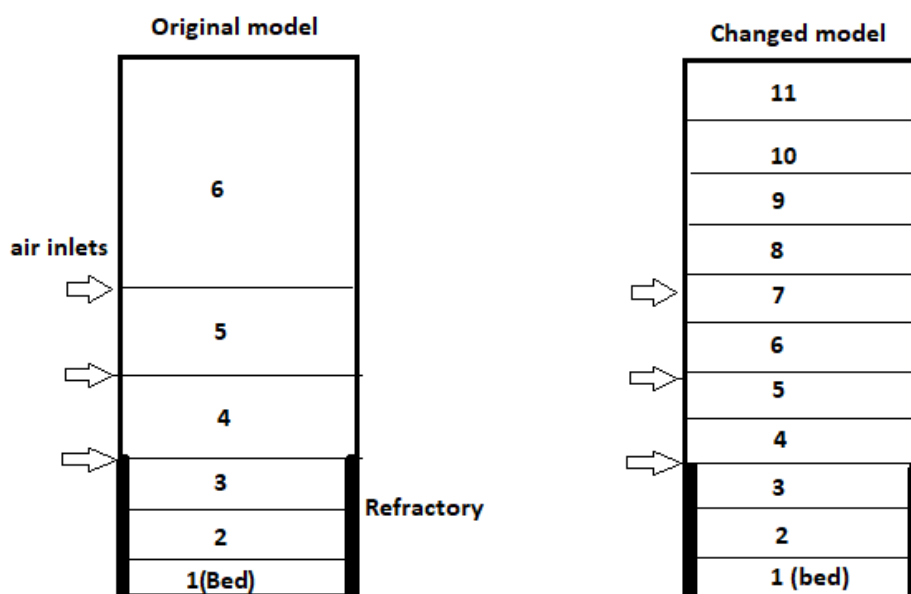


Figure 21. In the original model, volume elements in the freeboard were defined according to air inlet heights. In the changed model, element division is independent of air inlets.

This introduced inconsistencies in the mass balances and temperature profiles, as in some cases the air inlet could be near the end of a volume element, but the model would treat it as if the air had had time to mix in the same element. This meant the model was sensitive to the somewhat random element division, since a small change in the vertical position of

an element could cause the secondary air injection to move from one block to another. Because of this, the secondary air injections were rewritten in a way that would produce results proportional to the distance between the injection level and the element height coordinates.

Right before a secondary air injection, the flow can be thought to be mixed at a temperature T_1 . Given enough time after an air injection of air at temperature T_2 , the flow can again be thought to be mixed and at a uniform temperature T_3 . However, between these two well-mixed states, there is a transition period during which the two flows mix, and their local temperatures range between T_1 and T_2 before converging to T_3 . This transition was modelled by adding the injected air gradually into 3 downstream elements instead of the air being fed entirely into the first element, resulting in a temporary deficit in the mass balance that is corrected by the time the air injection is complete. This can be thought of being a compromise between injecting all the air in an element in which the air would not have time to mix and only injecting the air in the next element. The third element was included because in some cases the mixing of the injected air appeared to be slow, and an extra element was thought to be useful. The air flow injected in each of the three elements i is given by

$$q_{m,air,i} = q_{m,air}(I_i - \sum_j^{i-1} I_j) \quad (67)$$

where $q_{m,air}$ exceptionally refers to the air mass flow of one injection level
 I_i is an empirical parameter

The empirical parameter I estimates the share of air to be injected in the elements in question. It was thought that it should be dependent on the height from the air inlet to make the model less sensitive to the position of the inlet in relation to the element boundaries, and additionally dependent on the injection air mass flow, to account for faster mixing of high-speed injections, similar to what was done in chapter 4.4.2. The function chosen to estimate I was

$$I_i = \frac{(x_2 - x_1)k + e^{-k(x_2 - x_j)} - e^{-kb}}{(x_2 - x_1)k} \quad (68)$$

where x_j is the air injection height coordinate
 x_2 is the height coordinate of the upper boundary of the element
 x_1 is the height coordinate of the lower boundary of the element

$$b = \begin{cases} x_1 - x_j & \text{if } (x_1 - x_j) \geq 0 \\ 0 & \text{if } (x_1 - x_j) < 0 \end{cases}$$

$$k = a \frac{q_{m,air,i}}{q_{m,fg,i}}$$

a is an empirical parameter.

This function can be thought to depict the ratio of the area under an exponential curve of type $y(x) = 1 - \exp(-kx)$ to the total area of an element, as illustrated in Figure 22. The choice for the function used to estimate I is not particularly meaningful, as long as it produces a smooth transition between the state before the injection and the fully mixed state after the injection and allows for the curve to be easily tuned to match measurements, in this case by changing the parameter a .

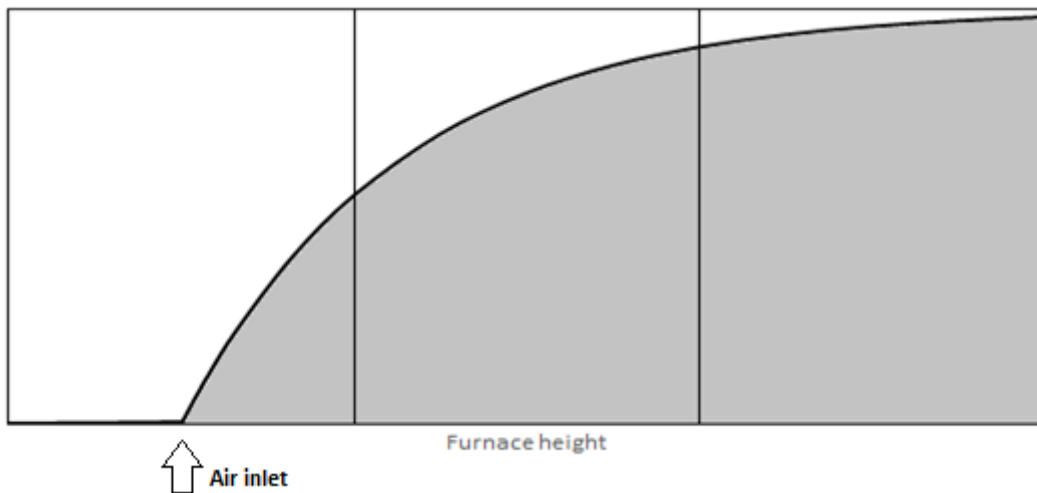


Figure 22. The air injection was split proportionally to the ratio of the grey area in each of the three elements under the exponential curve to the total element area.

The deficit in the mass balance of the first two elements after the air injection has four main effects on the results of the model: a reduced gas mass flow, reduced oxygen for combustion, increased gas temperature and changed heat transfer. The energy balance of an element in the freeboard is given by

$$q_{m,i-1}h_{i-1} + q_{m,air}h_{air} + Q_{comb} = q_{m,i}h_i + Q_{rad,net} + Q_{conv} \quad (69)$$

| | | |
|-------|---------------|--|
| where | $q_{m,i-1}$ | is the gas mass flow leaving the previous element |
| | h_{i-1} | is the specific enthalpy of the gas leaving the previous element |
| | $q_{m,air}$ | is the air mass flow entering the element |
| | h_{air} | is the specific enthalpy of the air entering the element |
| | Q_{comb} | is the heat released by combustion |
| | $q_{m,i}$ | is the gas mass flow leaving the current element |
| | h_i | is the specific enthalpy of the gas leaving the current element |
| | $Q_{rad,net}$ | is the net radiation out of the element |
| | Q_{conv} | is the convective heat transfer to walls in the element |

A reduction in the cold air mass flow injected into an element would result in an increase in the temperature of the element. However, this is balanced by the steeply increasing heat radiation, resulting in an overall small difference in temperature in most cases. This in turn would result in the next element being slightly colder after receiving the missing air mass flow than it would be without the splitting of secondary air injections, which results in this element emitting less radiation. Additionally, since the heat release function is strongly dependent on air injections as described in chapter 4.4, the effect that a cold air injection would have on the average temperature of an element is partly balanced by the increased heat release in the same element. All of these things combined result in the splitting of air injections having little effect on the overall heat balance of the furnace. It mainly influences the temperature of the element containing the air injection, and even then, it only produces significant changes if the air inlet is close to the upper boundary of the element in question.

4.4 Heat release function

The heat release model is divided into two parts, the freeboard and the bed area. In this work only the freeboard model was changed. The heat release profile of a freeboard is thought to depend mainly on the amounts of fuel and oxygen available and on their mixing, assisted by the turbulence caused by high-speed secondary and tertiary air inlets. An example of a heat release profile is shown in Figure 23.

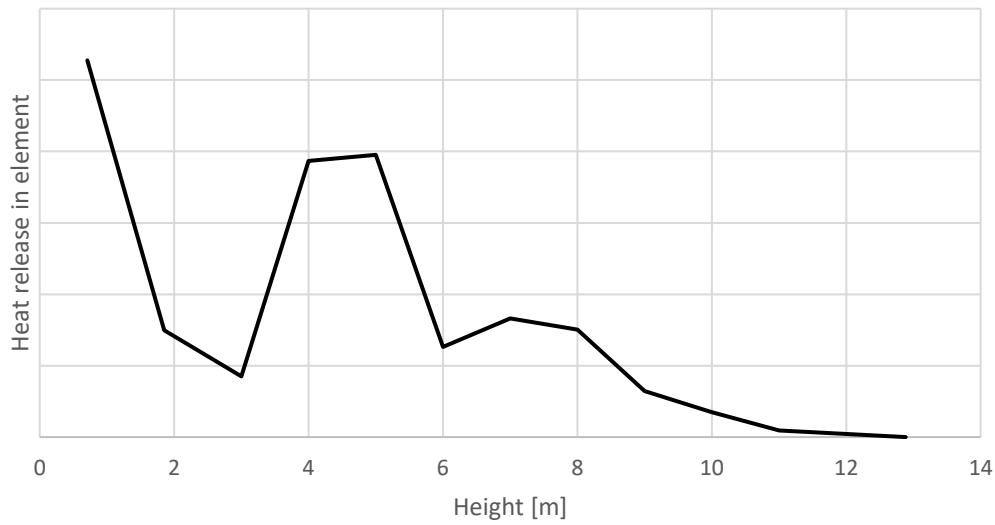


Figure 23. Heat release profile of case B3, with secondary air injection levels being at 3.5 m and 6.0 m.

It is assumed that the rate of combustion is proportional to the quantity of reactants available in an element, and happens as a function of mixing, which in turn is a function of downstream distance or furnace height x . Combustion is limited by oxygen and fuel supplies, and the first of these to be depleted is defined as reactant y

$$y = \min \frac{(q_{m,air,i}; q_{m,st,i})}{q_{m,st}} \quad (70)$$

where $q_{m,air,i}$ is the air mass flow in element i
 $q_{m,st,i}$ is the stoichiometric air needed to burn the fuel present in element i
 $q_{m,st}$ is the total air flow needed for stoichiometric combustion

The rate of change of y is then given by

$$\frac{dy}{dx} = -ky \quad (71)$$

where k is an undefined mixing constant

The solution for the differential equation above is

$$y(x) = Ce^{-kx} \quad (72)$$

where C is the integration constant

By inserting the initial condition $C = y(0) = y_0$ the equation becomes

$$y(x) = y_0 e^{-kx} \quad (73)$$

As defined in chapter 3.5, f_i is the ratio of heat released in element i to the maximum possible heat release in that element, limited by the combustion reactants. Since the quantity of reactants burned is equal to the change in their quantity, f_i can be written as

$$f_i(x) = \frac{X_i}{X_{\max,i}} = \frac{y_0 - y(x)}{y_0} = 1 - e^{-kx} \quad (74)$$

This exponential function is the core of the heat release function, and it has some interesting properties. The first is that it only receives values between 0 and 1 as long as x is non-negative, which is the range needed for a factor of this kind. The second is that it is memoryless, which means it is only dependent on its current state. For example, given an exponentially decreasing quantity $y(x) = y(0)e^{-x}$, its value at $x = a + b$ can be calculated directly using the initial condition $y(0)$, or it can be calculated without knowledge of a and $y(0)$ as long as $y(a)$ and b are known.

$$y(a + b) = y(0)e^{-(a+b)} = y(0)e^{-a}e^{-b} = y(a)e^{-b} \quad (75)$$

For comparison, for a logarithmically decreasing function $y^*(x)$ as given below,

$$y^*(x) = y^*(0)(1 - \ln(x + 1)) \quad (76)$$

calculating $y^*(a + b)$ only with the knowledge of $y^*(a)$ and b , but no knowledge of a or $y^*(0)$ would not be possible, since

$$y^*(a + b) = y^*(0)(1 - \ln((a + b) + 1)) \neq y^*(a)(1 - \ln(b + 1)) \quad (77)$$

This is illustrated in Figure 24., with the following definitions

$$y(b|a) = y(a)e^{-b} \quad (78)$$

and

$$y^*(b|a) = y^*(a)(1 - \ln(b + 1)) \quad (79)$$

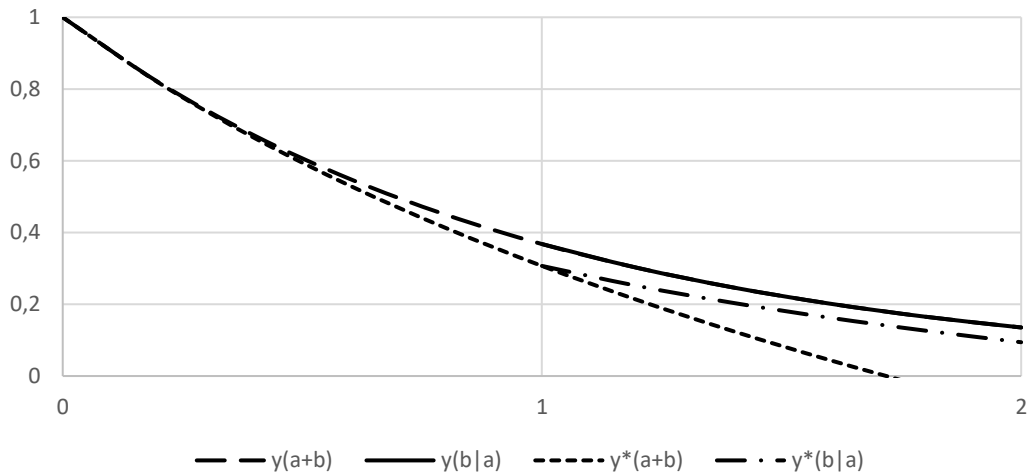


Figure 24. Demonstration of the memoryless property of the exponential function $y(x)$, which does not hold for the logarithmic function $y^*(x)$ with $a = b = 1$

What this property means in practice is that it allows the heat release function to be evaluated in an arbitrary number of parts, using only the most recent result to calculate the next. If a different function was used, the entire heat release profile would have to be generated at once. Otherwise it would produce different results depending on the number of divisions made, as was the case with the previous heat release function.

The third property is that the exponential function obtained approaches unity, but never truly reaches it. This is a minor mathematical detail as the difference would eventually be negligible, but it is interesting because this could be considered a viable way of describing the heat release in an idealised furnace operated at stoichiometric conditions, i.e. without excess air. However, real furnaces are operated at superstoichiometric conditions in order to reduce losses due to unburned fuel, which means the heat release function should be able to reach unity. Additionally, it means the amount of oxygen in the upper parts of the furnace should influence the heat release profile, but this is not currently the case as the heat release function given above is only a function of the limiting reactant i.e. the fuel, of the undefined mixing coefficient k , and of downstream distance x . To better reflect the effect that the air ratio has on combustion, the fuel-to-air factor was introduced.

4.4.1 The fuel-to-air factor

A concentrated secondary air injection could be imagined expanding homogeneously until it fills the entire container volume, as shown in Figure 25. This naturally results in the mass concentration of the injection air decreasing not to violate conservation of mass, according to

$$m_{\text{air}} = \rho_{\text{air}} V_{\text{air}} \quad (80)$$

where m_{air} is the mass of air present
 ρ_{air} is the mass concentration of air [kg/m^3]
 V_{air} is the volume the air injection has spread into

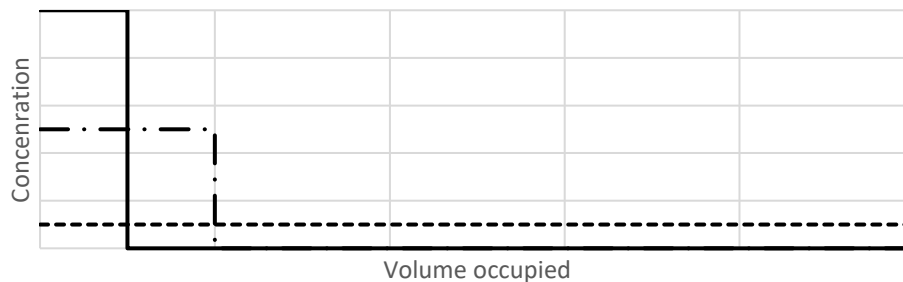


Figure 25. Idealised homogeneous expansion of a gas injected in a volume, where the system is depicted shortly after injection of air (solid line), in a fully mixed state (dashed line), and in an intermediate state (dash-dotted line).

If the flue gas volume and the expanding air injection volume in a substoichiometric furnace were assumed to be independent continua, and if the combustion of gaseous volatiles was assumed to be restricted only by their mixing with oxygen, combustion would happen where the two phases overlap. Additionally, due to both fuel and oxygen being quantified in the model by means of the total stoichiometric air needed in the furnace, they are consumed in equal amounts. If the fuel mixture is assumed to be homogeneously mixed over the entire volume, the point at which the injected air has expanded enough to be fully consumed by combustion is the point where both fuel and air exist in equal amounts in the same space. This is equivalent to the concentrations of both phases being equal, as illustrated in Figure 26.

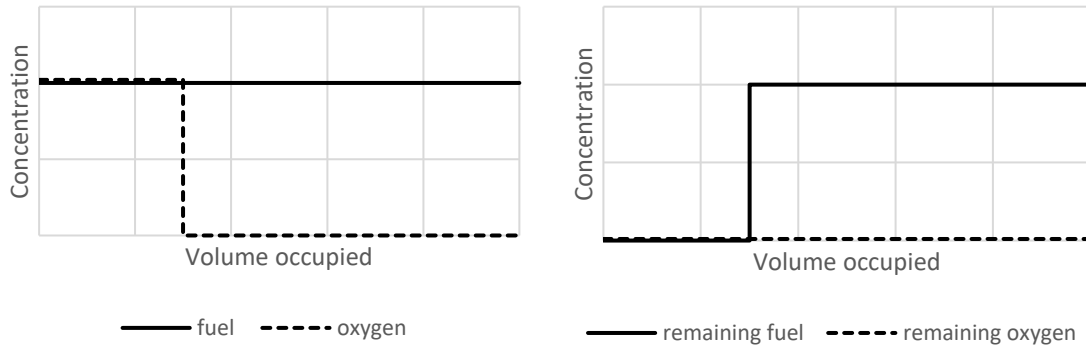


Figure 26. Idealised depletion of injected air, before and after a discrete combustion event. The mass of both phases in the volume bounded by the dashed line in the picture on the left are equal, since $m = \rho V$.

By defining mixedness as the fraction of the total volume the injected air has spread into, i.e.

$$M = V_{\text{air}}/V_{\text{tot}} \quad (81)$$

a gaseous air-fuel mixture with an air coefficient of 1.0 in this idealised system would fully react when the injected air has spread to occupy the entire volume, i.e. when the system is fully mixed. Since the stoichiometric air needed to burn the fuel present (m_{st}) is a measure for the amount of fuel in an element, the fuel-to-air ratio F can be defined as the ratio

$$F = \frac{m_{\text{st}}}{m_{\text{air}}} \quad (82)$$

Since the concentration of both phases is equal at the point in which the injected air has spread enough to be fully consumed, and since $\rho = m/V$, complete air consumption happens when

$$\frac{m_{\text{st}}}{V_{\text{tot}}} = \frac{m_{\text{air}}}{V_{\text{air}}} \quad (83)$$

By using equation 82 to express m_{st} in terms of F and m_{air} , the above equation can be rearranged to find the mixedness required to fully consume the injected oxygen, as below

$$M = \frac{V_{\text{air}}}{V_{\text{tot}}} = \frac{1}{F} \quad (84)$$

If one assumes that mixedness $M(x)$ approaches a fully mixed state $M(x) = 1$ exponentially as a function of downstream distance x traversed and at a rate k_2 , it could be expressed as

$$M(x) = 1 - e^{-k_2 x} \quad (85)$$

Due to its exponential nature, a fully mixed state would never be reached. However, the mixedness can eventually reach the value of $1/F$ needed for complete heat release as long as $F > 1$, i.e. in substoichiometric conditions, as shown in Figure 27. Note that complete heat release is defined as complete oxygen depletion in this case.

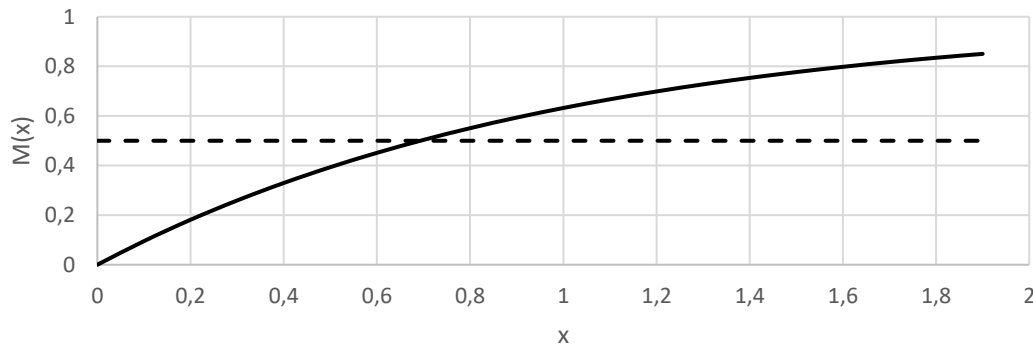


Figure 27. Increase of mixedness as a function of downstream distance (solid line) and the mixedness required for complete heat release if $F = 2$ (dashed line).

If x_d is the downstream distance needed for complete depletion of oxygen, then

$$M(x_d) = (1 - e^{-k_2 x_d}) = F^{-1} \quad (86)$$

This is also the point at which the heat release coefficient $f(x)$ should be equal to 1

$$f(x_d) = 1 - e^{-k x_d} = 1 \quad (87)$$

The exponential function of $f(x)$ is incapable of reaching a value of one in its current form. Since it was written with the assumption that combustion was determined by the mixing of combustible gases with oxygen, it can be rewritten to fulfil equations 86 and 87 as following

$$f(x) = F M(x) = F(1 - e^{-kx}) \quad (88)$$

If a superstoichiometric amount of air was injected into the idealised system shown in Figure 26, full heat release would not happen until the injection was fully mixed. However, if the phases were reversed, and the fuel mixture was thought to spread into the air phase instead, complete fuel burnout would be achieved when

$$M(x_d) = F = \frac{m_{\text{air}}}{m_{\text{st}}} \quad (89)$$

By further expressing the air and fuel masses using mass flows instead, as used in the model, equation 88 could be extended to be valid in all conditions by defining F as

$$F = \frac{\max(q_{m,\text{air},i}; q_{m,\text{st},i})}{\min(q_{m,\text{air},i}; q_{m,\text{st},i})} \quad (90)$$

where $q_{m,\text{air},i}$ is the air mass flow in element i
 $q_{m,\text{st},i}$ is the stoichiometric air mass flow needed for full fuel consumption in element i

There are two limitations to the expression obtained for the heat release coefficient. The first is that $f(x)$ can produce values between $0 \leq f(x) < F$, as opposed to the previous range $0 \leq f(x) < 1$, which means an additional condition had to be written to limit $f(x)$ to values not higher than one. The second limitation is the singularity in the denominator of F as y approaches zero due to oxygen or fuel burnout. This was solved by giving F an arbitrary maximum possible value of 1000.

The solution found is interesting, as when inserted in equation 44 to find the total heat released it yields

$$X_i = X_{i,\text{max}} f_i = \frac{\min(q_{m,\text{air},i}; q_{m,\text{st},i})}{q_{m,\text{st}}} \frac{\max(q_{m,\text{air},i}; q_{m,\text{st},i})}{\min(q_{m,\text{air},i}; q_{m,\text{st},i})} (1 - e^{-kx}) \quad (91)$$

meaning the limiting reactant $y = \min(q_{m,\text{air},i}; q_{m,\text{st},i})$ has no impact on the heat release rate, and only serves as an upper limit for the total heat released.

4.4.2 Mixing rate

Since the term $(1 - e^{-kx})$ in the expression for the heat release coefficient describes mixing as a function of downstream distance x , the coefficient k includes the main factors that affect the rate of mixing. Based on existing research on mixing presented in chapters 2.4.2 and 2.5.1, the factors included are the jet momentum flux ratios J of air injections and the dimensionless downstream distance x/D , i.e., the ratio of downstream distance to furnace depth, assuming the air is injected from the front and rear walls, however the dimensionless downstream distance x/D was changed to a simple downstream distance x as it appeared to produce better results. Additionally, a constant was included to account for small-scale turbulence and mixing unrelated to air inlets.

However, the model does not currently include secondary air nozzle dimensions and numbers, nor jet velocities. Instead of increasing the number of required inputs for the model, J was written as function of injected air mass flows according to

$$J = \frac{v_j^2 \rho_j}{v_c^2 \rho_c} = \left(\frac{A_c}{A_j} v_j \right) \frac{q_{m,j}}{q_{m,c} v_c} \quad (92)$$

| | | |
|-------|----------|--|
| where | A_c | is the crossflow cross-section area |
| | A_j | is the sum of nozzle inlet areas of an injection level |
| | v_j | is the air jet velocity |
| | v_c | is the crossflow velocity, i.e. flue gas flow velocity |
| | ρ_j | is the air jet density |
| | ρ_c | is the crossflow density |

The mass flows and the average crossflow velocity are calculated by the model. The ratio A_c/A_j appeared to vary in the 200~300 range for the cases studied, and a typical constant value was used for the jet inlet velocity. In the region before the first secondary air level, mixing is thought to depend mainly on the jets of fuel feeding air and start burners. While the secondary and tertiary air inlets are arranged in a way that maximises mixing, this may not be the case in the region below them. Poor mixing is thought to be caused mainly by lower inlet velocities and wider spacing between nozzles. As such, the effect of air

injections in the form of fuel feeding air and start burners in the lower furnace was decreased by lowering the value of the coefficient $A_c/A_j \cdot v_j$ to one tenth of the value used in the upper furnace area.

However, there are a number of inaccuracies in the calculation of these values. Firstly, the area ratios and the jet inlet velocities were obtained at full load. At partial loads, the volumetric flow of air injections can be significantly lower, which results in an overestimation of J by the model. Secondly, the model uses the mass flow injected into the element in question to calculate J and the rate of mixing, but the mass flow injections in the model were split into three downstream elements as described in chapter 4.3. This means that the model essentially calculates three values of J for three smaller air injections in three elements, as opposed to one J for the entire inlet level. If the examples found in literature were to be followed more rigorously, J would be calculated at the jet inlet, and this value would be the basis for the calculation of mixedness in the downstream elements until the next air inlet was reached. If nozzles are implemented in the model in more detail in the future, the calculation of J could also be revised.

Under these assumptions, and by defining Δx_i as the height of element i , the correlation for the heat release coefficient is

$$f_i = F_i(1 - \exp(-(J_i^a + b)c\Delta x_i^d)) \quad (93)$$

and J is given by

$$J = \tilde{a} \left(\frac{A_c}{A_j} v_j \right) \frac{q_{m,j}}{q_{m,c} v_c} \quad (94)$$

where $q_{m,j}$ is the air mass flow being injected into the element
 $q_{m,c}$ is the flue gas mass flow of the previous element
 v_c is the flue gas velocity of the previous element

and a , b , c , d , and \tilde{a} are correction parameters used to fit the correlation to measurements. The value of $\frac{A_c}{A_j} v_j$ was estimated to be higher for the secondary and tertiary air injections than for the injections below them, i.e. for start burners and fuel feeding air. The fitting

was done manually, and no specific optimisation techniques were used, which means a better fit could be found.

4.4.3 Entrained fuel combustion

The heat release of entrained fuel was previously estimated to be evenly distributed between all elements, which made it dependent on the placement of calculation blocks. It is now rewritten in a way similar to the heat release of gaseous fuel in order to make it grid independent. The entrained fuel was thought to consist of mainly solid particles with a certain share of fixed carbon, and consequently was thought to have longer combustion times and burn mainly in the main combustion zone between secondary air levels or above. The correlation used for the entrained fuel combustion share $f_{i,entr}$ was

$$f_{i,entr} = \left(1 - \exp \left(-(J^{a'} + b') \frac{q_{m,fg,i}}{q_{m,fg,tot}} \Delta x_i c' \right) \right) F^{d'} \quad (95)$$

where $q_{m,fg,i}$ is the flue gas mass flow in element i
 $q_{m,fg,tot}$ is the total flue gas mass flow at furnace exit
 Δx_i is the element height

J and F are defined as previously, and a' , b' , c' , and d' are fitting. The ratio $q_{m,fg,i}/q_{m,fg,tot}$ was included to limit the combustion of solids in the lower parts of the furnace. It has no theoretical background and is essentially another fitting parameter.

The heat released by entrained fuel combustion $Q_{entr,i}$ is then given by

$$Q_{entr,i} = Q_{fuel} s_{entr} f_{i,entr} \quad (96)$$

where Q_{fuel} is the total energy in the fuel
 s_{entr} is the entrained fuel share

4.5 Gas absorptivity correlation

When the predictive capabilities of the model are considered, its ability to accurately calculate the total heat transfer to walls is crucial, and this in turn is dominated by

radiation. This means that the overall heat transfer to walls would have to be calculated with sufficient accuracy so that the correction factor could be kept at 1.

During model testing, higher radiation correction factors were observed for part-load simulations than for full-loads in general. Upon closer inspection, it was found that the calculated gas absorptivity was significantly lower for part-load runs, and the reason for this was investigated. While it is an important part of the overall functionality of the model, only minor changes were made to the gas absorptivity correlation due to time constraints.

The correlation for gas absorptivity a_c by Keltanen (2007) that was used in the model is given below

$$a_c = be^{cx_c} \quad (97)$$

where b is an empirical parameter
 c is an empirical parameter
 x_c is an estimate for the flue gas dust content, defined as

$$x_c = a \frac{q_{m,fg,tot}}{V_{freeb}\lambda} = a \frac{v_f \rho_g}{H_{furn}\lambda} \quad (98)$$

where $q_{m,fg,tot}$ is the total flue gas mass flow at furnace exit
 V_{freeb} is the freeboard volume
 λ is the air coefficient
 v_f is the flow velocity at furnace exit
 ρ_g is the gas density at furnace exit
 H_{furn} is the furnace height
 a is an empirical parameter

As can be seen, x_c is directly proportional to the flue gas flow velocity. Since the gas flow is lower at smaller loads, this caused the estimated gas absorptivity to be lower as well, which required a higher correction factor. Since the model underpredicted the radiation in part-load cases, x_c was rewritten as

$$x_c = a\bar{v} \frac{\rho_g}{H_{\text{furn}}\lambda} \quad (99)$$

where \bar{v} is a typical exit velocity for a furnace at full load

According to Chew et al. (2015), most solids elutriation correlations in literature predict an increase in the solids elutriation rate with increased flow velocity, which would suggest the inclusion of the velocity term being justified. However, the increased flow velocity would also increase the volumetric gas flow. Since the solids elutriation rate depicts the mass flux of solids, i.e. the mass of solids crossing a cross-section equal to a square metre every second ($\text{kg}/\text{m}^2\text{s}$), the solids loading (in kg/m^3) is obtained by dividing the elutriation rate by the flow velocity. This results in the higher elutriated solid mass being spread over a larger volume if the flow velocity is increased, and in the solids loading not increasing as much as the elutriation rate does. In the end, the approach that produced results more in line with measurements was selected, and the part-load gas absorptivity was increased to the level of full loads. This resulted in a significant reduction of the correction factors needed for part-load cases.

4.5.1 Comparison with entrainment correlations

The estimation of the solids load in the freeboard using correlations found in literature was also explored. This was done in order to cross-check the gas absorption coefficients obtained, and to acquire a better understanding of particulate radiation in the freeboard.

According to the method described in chapter 2.1.3, the mass flux [$\text{kg}/\text{m}^2\text{s}$] of solids ejected from the bed surface is thought to be dominated by particles ejection caused by bubble eruptions. The solids mass flux then declines exponentially as function of furnace height until the elutriation rate of fine particles F_∞ is reached. However, the elutriation rate obtained produced a solids mass flow three orders of magnitude lower than the ash mass flow calculated for these furnaces, which is thought to be mainly fly ash. As reported by Chew et al. (2015), different solids elutriation correlations can produce results varying by up to 20 orders of magnitude. If the ash flow is considered a minimum value for the solids flow in the upper freeboard, using the ash flow to estimate the elutriation of solids could be a more reliable approach. F_∞ can then be estimated to be

$$F_{\infty} \left[\frac{\text{kg}}{\text{m}^2\text{s}} \right] = \frac{q_{\text{m,ash}}}{A_c} \quad (100)$$

where A_c is the furnace cross-section
 $q_{\text{m,ash}}$ is the ash mass flow

The solids load profiles obtained decreased exponentially for the first four meters above the bed surface until the constant elutriation rate was reached. Gas absorptivity coefficients were calculated according to VDI (2010, pp. 989–998), producing high coefficients for the first two to three meters above the bed surface, which then decreased to a constant absorptivity value in the upper freeboard. These results are in line with what was expected, and while the deviation is small, they produced consistently higher volume-averaged absorptivities than predicted by the absorptivity correlation of the model for the four cases evaluated, as is shown in Table 3.

Table 3. Comparison of gas absorptivities obtained by applying methods found in literature and absorptivities estimated by the model

| Case | Methods found in literature | Model correlation |
|------|-----------------------------|-------------------|
| B1 | 0.24 | 0.21 |
| B3 | 0.25 | 0.22 |
| C1 | 0.20 | 0.17 |
| A1 | 0.15 | 0.09 |

The values obtained are in no way definitive, but merely an estimation, as time constraints did not allow for a deeper understanding of these methods. However, these new results would appear to be indirectly supported by measurements, as the average radiation correction factor used in the back-calculated cases is higher than 1.0, suggesting that radiation is currently underestimated by the model.

An explanation for the underestimation of radiation could be the generally lower temperatures modelled currently, as consequence of the inclusion of afterburning. The model would previously produce a hotter temperature profile, which would result in smaller gas absorptivity values being obtained in the process of fitting the radiative heat flux to the temperature profile.

Additionally, it is possible that the larger difference in the gas absorptivity of Case A1 is due to its height being outside the validity range of the correlation. Assuming the solids loading to decrease exponentially during the first few metres above the bed surface down to the constant value given by the fines elutriation rate as shown in Figure 28, the volume-weighted average solids loading of the shorter furnace would be higher due to the height of the dense splash region being roughly constant.

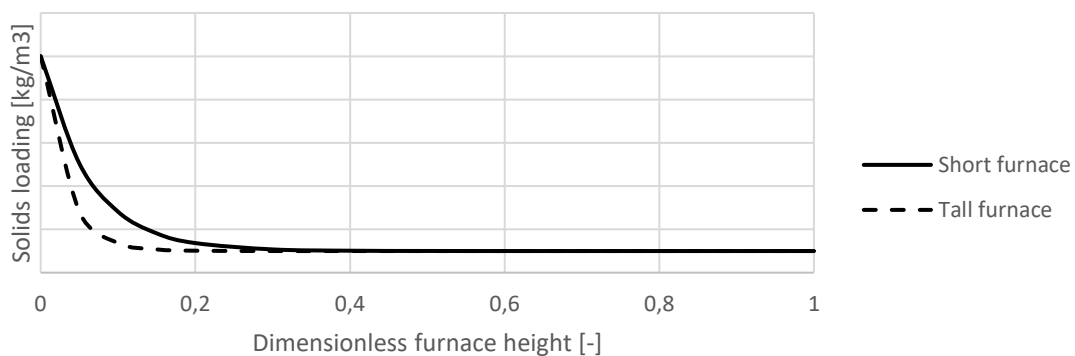


Figure 28. Qualitative depiction of the solids loading of a tall and a short furnace as function of dimensionless height.

It is thought that the furnace height term H_{furn} in the model correlation is used to estimate the effect the furnace height has on the average solids loading. However, it causes the overall average to approach zero instead of the fines elutriation rate F_{∞} . Assuming the average solids loading of a furnace to be similar to the ratio of a constant to the furnace height, i.e. c/H , may result in the underestimation of solids loadings for tall furnaces, as shown in Figure 29.

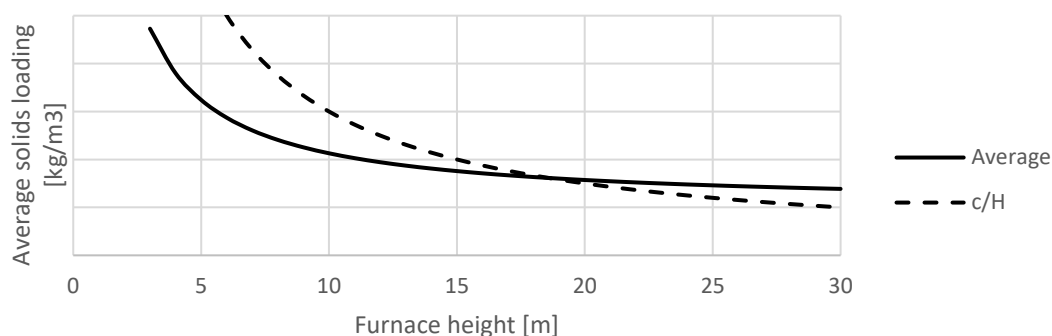


Figure 29. Average solids loadings as function of furnace height compared to estimate by c/H .

Another way the gas absorptivity currently used may impact the radiation correction factor needed is through the assumption of a constant gas absorptivity. The estimation of the measurement error of a thermocouple is dependent on the optical thickness of the gas body it is in. A thick gas would cause the thermocouple to exchange radiation only with the surrounding gas, while a thin gas would allow the thermocouple to see more distant elements, such as the bed and walls. The average gas absorptivity is likely higher than the local absorptivity of the real gas in the upper regions of the freeboard. This means that the steep temperature gradient measured in the upper freeboard may be partially caused by radiation between the thermocouple and the cold furnace walls being stronger than estimated by the model, which results in a bigger correction factor being needed. Similarly, the temperatures measured in the lower freeboard are likely closer to the true gas temperature, since the gas-solids suspension is thought to be denser there.

Based on the material presented in this chapter, a revision of the estimation of gas absorptivity would probably be the single most efficient way of improving the predictive capabilities of the model.

5 RESULTS

The validation process was done in two steps: first, the post-combustion factor and the radiation correction factor were adjusted manually to fit the furnace exit gas temperatures (FEGTs) to measured values in a way that would also satisfy the boiler energy balance. This gives the temperature profiles obtained if one was to perform back calculations on the existing furnaces. The second step was to evaluate how accurate the predictive use of the furnace model would be by using the post-combustion correlation and averaged radiation correction factors. Using a constant correction factor resulted in mean temperature errors decreasing with furnace height for full loads and increasing for part loads. The correction factors finally selected were smaller for full loads, increasing linearly up to a maximum value for half-load cases. Two of the predicted profiles generated are shown below in Figure 30 and Figure 31.

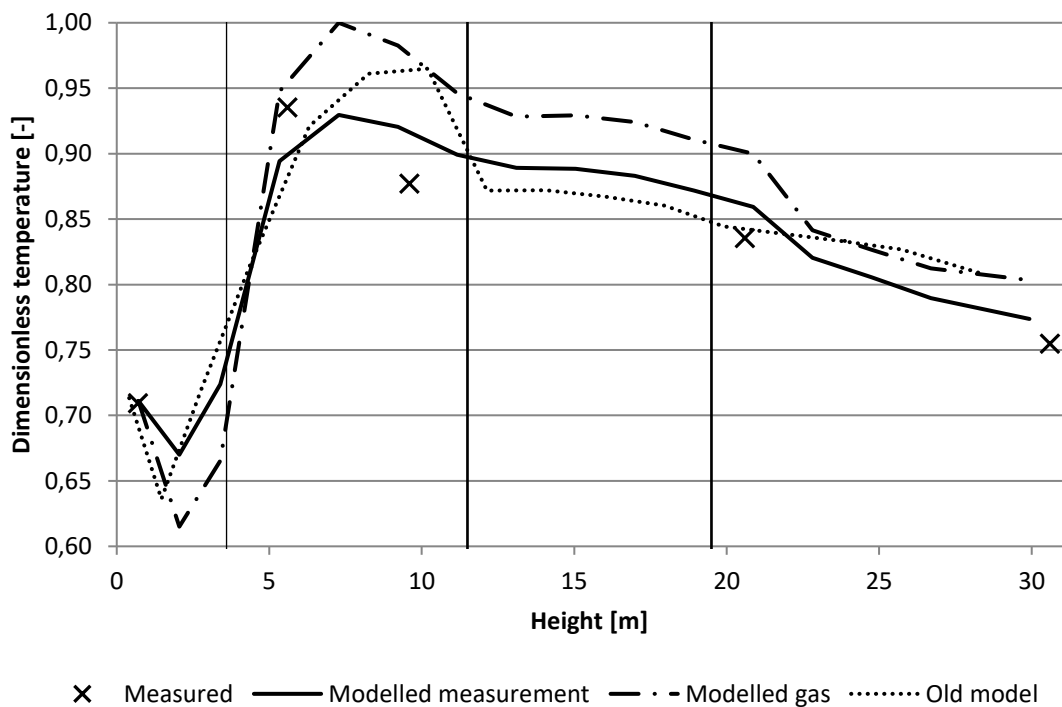


Figure 30. Generated temperature profiles for Case A1. Vertical lines depict air injection levels.

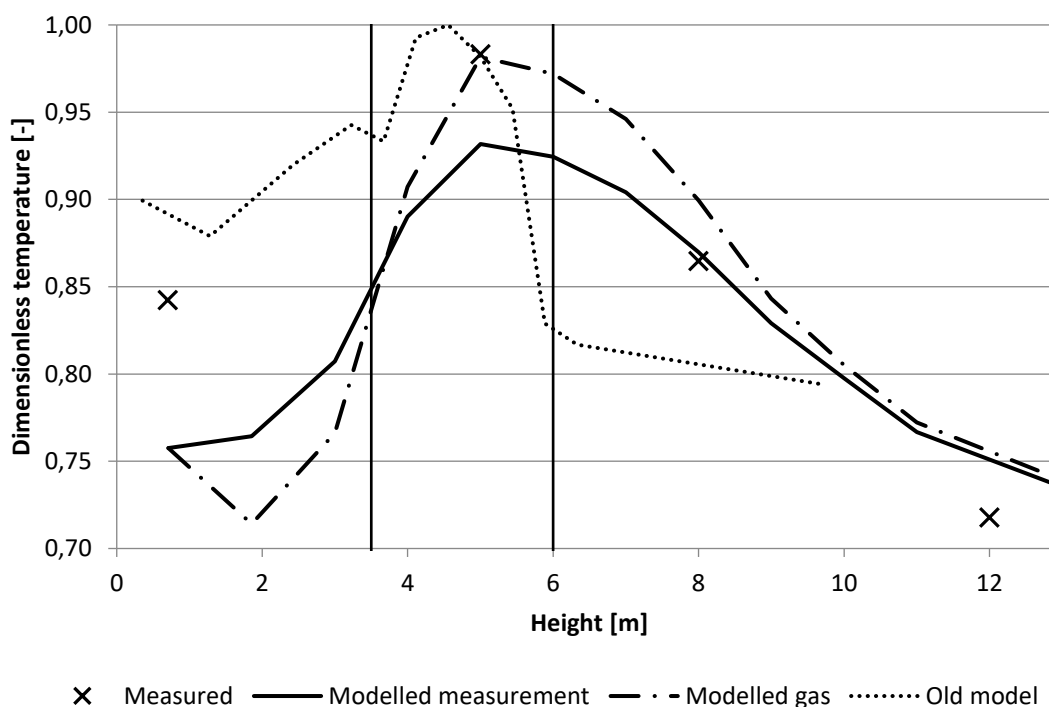


Figure 31. Generated temperature profiles for Case B2. Vertical lines depict air injection levels.

The difference between the modelled gas temperature and the modelled measurement temperature comes from the estimation of the measurement error, as described in chapter 4.1. If measurements of the same furnace are available at different depths, the deepest results were used as they are thought to best reflect the average temperature of the furnace.

The cases above were chosen to show different extremes, with Boiler A1 being a large furnace with a high share of fines in its fuel, while Boiler B2 is a part-load run of a small furnace. Most other cases produce comparable results, but there were two exceptions. Boiler B5 and Boiler C4 were difficult cases, and it is thought there is some kind of error in their back-calculation or measurement. The radiation correction factor and the post-combustion factor needed for Boiler B5 in the back calculation were about three times as high as what would be expected on average, while Boiler C4 also required a high post-combustion factor. In predictive calculations, both cases saw unusually high error levels throughout the furnace area, while for all other cases the largest error levels were in the lower furnace, as illustrated in Figure 32.

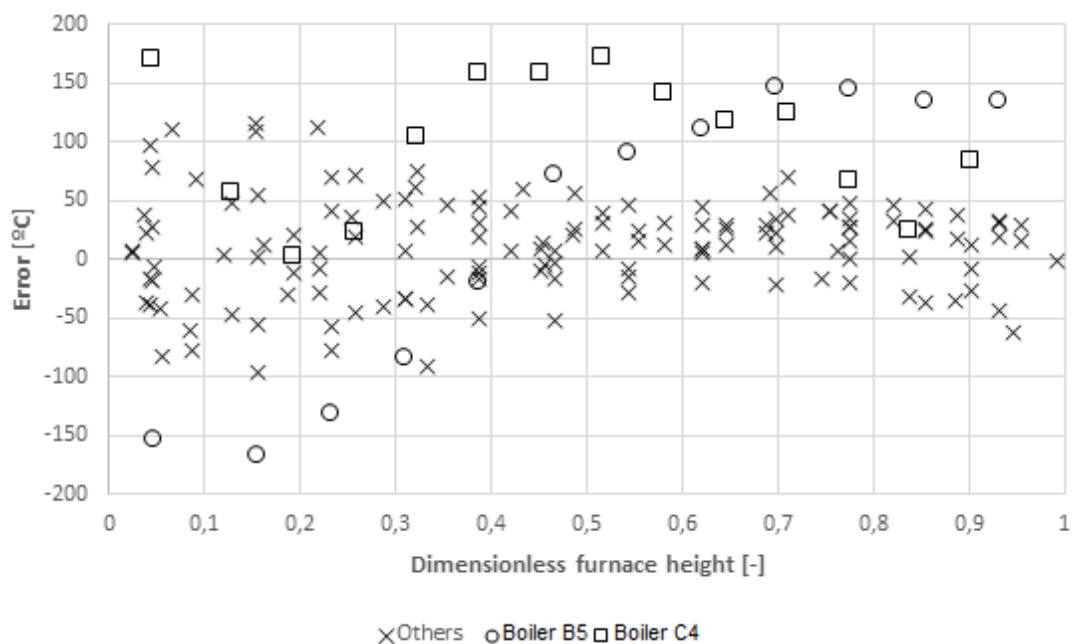


Figure 32. Difference between measured temperatures and the closest modelled temperatures as function of dimensionless furnace height for the outliers Boiler B5 and Boiler C4, and for the remaining cases.

The results obtained for all cases are compared with the back-calculated results obtained with the old furnace model in Table 4 and Table 5. The cases back calculated with the old model were A 1, B 1–4 and C 1–2.

Table 4. Difference between measured temperature and closest modelled temperatures in the bed and the freeboard. MBE = mean bias error, MAE = mean absolute error, SD = standard deviation. Cases B 5 and C 4 were considered outliers.

| Calculation type | Bed error [°C] | | | Freeboard error [°C] | | |
|-----------------------|----------------|------------|-----------|----------------------|------------|-----------|
| | <i>MBE</i> | <i>MAE</i> | <i>SD</i> | <i>MBE</i> | <i>MAE</i> | <i>SD</i> |
| New predictions | | | | | | |
| All cases | 1.8 | 53.5 | 50.7 | 15.7 | 46.2 | 28.1 |
| Excluding outliers | 1.0 | 38.1 | 30.3 | 8.4 | 38.0 | 18.0 |
| New back calculations | | | | | | |
| All cases | -24.1 | 57.7 | 40.0 | 0.0 | 42.0 | 23.3 |
| Excluding outliers | -19.8 | 53.8 | 35.5 | -2.6 | 36.7 | 19.5 |
| Old back calculations | 70.5 | 77.5 | 98.3 | 66.6 | 91.6 | 51.2 |

Table 5. Error between modelled and actual FEGT and maximum temperature in the furnace. MBE = mean bias error, MAE = mean absolute error, SD = standard deviation. Cases B 5 and C 4 were considered outliers. (*) FEGT error between required value for boiler heat balance and virtual FEGT. Not given for back-calculations since they were manually matched.

| Calculation type | Peak temp. error [°C] | | | FEGT error (*) [°C] | | |
|-----------------------|-----------------------|------------|-----------|---------------------|------------|-----------|
| | <i>MBE</i> | <i>MAE</i> | <i>SD</i> | <i>MBE</i> | <i>MAE</i> | <i>SD</i> |
| New predictions | | | | | | |
| All cases | 4.8 | 40.3 | 27.5 | -17.0 | 66.6 | 49.5 |
| Excluding outliers | 3.8 | 38.2 | 28.5 | -13.5 | 52.8 | 32.5 |
| New back calculations | | | | | | |
| All cases | -16.3 | 45.3 | 31.7 | - | - | - |
| Excluding outliers | -9.0 | 42.1 | 30.3 | - | - | - |
| Old back calculations | 95.5 | 95.5 | 73.4 | - | - | - |

As can be seen, the error level decreased drastically when compared to the older back calculations, though it should be noted that the cases back-calculated using the old model were outside its validity range regarding furnace type and size. The new model appears to predict the bed and peak temperatures fairly accurately, as can be seen from their mean errors, but it seems to slightly overestimate radiation and the mean temperature in the freeboard since the obtained FEGTs were generally too low. The precision of the model appears to be in the order of 40–50 °C for the most part, with its ability to correctly predict the FEGT being slightly worse. The FEGT error being higher is interesting, since typical use of the model involves matching the FEGT produced by the model to the FEGT required to satisfy the boiler heat balances, for example by changing the radiation correction factor. However, since the FEGT calculated by the model has a higher mean absolute error level than the rest of the furnace, including the calculation of the FEGT in the process of solving the furnace temperature may result in higher error levels throughout the furnace. The FEGT calculated by the model cannot be ignored, but in light of the results presented in this chapter, it may be useful to also solve the furnace temperatures using average correction factors and then compare results.

While the results produced are better, there are still inaccuracies in the model, even on a qualitative level. It is known from practical experience that increasing the grid air flow

enhances combustion and increases the bed temperature. While the model increases the heat generated in such cases, this change is not sufficient to overcome the higher convective heat flow resulting from a higher gas mass flow out of the bed, and this causes the bed temperature to cool. This is apparent when the cases B 1 and B 5 are compared, with B 5 having a higher grid air flow rate but lower bed temperature. While case B 5 produced unusually high error rates in general, the exact reason for this is not known, and it may be at least partially due to this inaccuracy in the bed area heat release.

Additionally, many generated temperature profiles show deep drops in temperature just above the bed. This appears to be caused by an overestimation of evaporation above the bed, combined with a generally low heat release rate in the elements in question. If a more accurate model is needed for the bed region, a review of bed area heat release and moisture evaporation could be useful.

6 SUMMARY

The first major objective of this work was to develop the existing 1D model to produce more reliable results especially in the upper regions of the furnace, so that it could be used as a tool in the placement of ammonia injection levels and in determining the residence time of flue gases of waste incineration plants. The second major objective was to improve its accuracy and validate it for the modelling of part-load runs. The approach used to reach these goals consisted of studying related material available in literature and studies conducted by Sumitomo SHI FW, followed by application of this newfound knowledge in the model itself. Finally, the obtained results were validated against the newest available measurement data.

Improvements were made in both areas and the resulting temperature profile is more accurate, though it is not yet clear whether it is accurate enough to be used according to the first objective. The air injections being split across several elements seems to better reflect their influence on the measured temperature profiles, and the new heat release correlation is able to estimate the increase in temperature based on air injections and unburnt fuel. The estimation of measurement errors due to radiation, combined with the modelling of afterburning was able to reduce the discrepancy between measured and modelled temperatures, while the change made to the gas absorptivity correlation reduced the difference between the correction factor needed for full and part loads.

The highest error levels observed were in the lower freeboard and in the estimation of the furnace exit gas temperature, however the former is not particularly meaningful for the applications that motivated this work. The estimation of the furnace exit gas temperature is dependent on the predicted radiative output into the furnace walls, which appears to be underestimated due to the gas absorptivity correlation being outdated.

A more detailed study of the gas absorptivity and of radiation inside BFB furnaces in general appears to be the most important step to be taken in future development of the model if higher precision is required for the upper freeboard. If precise modelling of the bed and of the lower freeboard is needed, further development of the bed area heat release correlation and the moisture evaporation sub model would be required.

REFERENCES

Chew, J.W., Cahyadi, A., Hrenya, C.M., Karri, R. & Cocco, R.A. 2015, 'Review of entrainment correlations in gas-solid fluidization', *Chemical Engineering Journal*, vol. 260, pp. 152–171.

Choi, C., Choi, W., Choi, J.H., Shin, D. 2016, 'Penetration behavior of opposed rows of staggered secondary air jets depending on jet penetration coefficient and momentum flux ratio', *International Journal of Heat and Mass Transfer*, vol. 101, pp. 274–279.

Darton R., LaNauze, R., Davidson, J.F. & Harrison, D. 1977, 'Bubble-growth due to coalescence in fluidized-beds', *Trans. I. Chem. Engrs.*, vol. 55, pp. 274–280.

Dioguardi, F. & Mele, D. 2015, 'A new shape dependent drag correlation formula for non-spherical rough particles. Experiments and results', *Powder Technology*, vol. 277, pp. 222–230.

Geldart, D. 1973, 'Types of Gas Fluidization', *Powder Technology*, vol. 7, pp. 285–292.

Haberle, I., Haugen, N.E.L. & Skreiberg, Ø. 2018, 'Combustion of Thermally Thick Wood Particles: A Study on the Influence of Wood Particle Size on the Combustion Behavior', *Energy & Fuels*, vol. 32, no. 6, pp. 6847–6862.

Holdeman, J.D., Smith, T.D., Clisset, J.R. & Lear, W.E. 2005, *A Spreadsheet for the Mixing of a Row of Jets with a Confined Crossflow*, Glenn Research Center, National Aeronautics and Space Administration.

Holdeman, J.D., Clisset, J.R. & Moder, J.P. 2010, *Spreadsheet Calculations for Jets in Crossflow: Opposed Rows of Inline and Staggered Holes and Single and Opposed Rows with Alternating Hole Sizes*, Glenn Research Center, National Aeronautics and Space Administration.

Holdeman, J.D. 2016, 'Re: Penetration behavior of opposed rows of staggered secondary air jets depending on jet penetration coefficient and momentum flux ratio', *International Journal of Heat and Mass Transfer*, vol. 102, pp. 435–444.

Horio, M. 2010, 'Fluidization Science, its Development and Future', *Particuology*, vol. 8, no. 6, pp. 514–524.

Ikonen, J. 2004, *Development of Furnace Model for Bubbling Fluidized Bed Boiler*, Department of Energy and Environmental Technology, Lappeenranta University of Technology.

Keltanen, J. 2007, *Development and Validation of Bubbling Fluidized Bed Furnace Model*, Department of Energy and Environmental Technology, Lappeenranta University of Technology.

Koornneef, J., Junginger, M., Faaij, A. 2007, 'Development of fluidized bed combustion—An overview of trends, performance and cost', *Progress in Energy and Combustion Science*, vol. 33, no. 1, pp. 19–55.

Li, J. & Kwauk, M. 1994, *Particle-Fluid Two-Phase Flow: The Energy-Minimization Multi-Scale Method*, Metallurgical Industry Press, Beijing.

Modest, M.F. 2013, *Radiative heat transfer*, 3rd edition, Elsevier Science, San Diego.

Momenikouchaksaraei, M. 2013, *Fundamental Study of Single Biomass Particle Combustion*, Department of Energy Technology, Aalborg University.

Niklasson, F., Thunman, H., Johnsson, F. & Leckner, B. 2002, 'Estimation of Solids Mixing in a Fluidized-Bed Combustor', *Ind. Eng. Chem. Res.*, vol. 41, no. 18, pp. 4663–4673.

Olsson, J., Pallarès, D., Johnsson, F. 2012, 'Lateral fuel dispersion in a large-scale bubbling fluidized bed', *Chemical Engineering Science*, vol. 74, pp. 148–159.

Rabi, J.A. & de Souza-Santos, M.L. 2003, 'Incorporation of a Two-Flux Model for Radiative Heat Transfer in a Comprehensive Fluidized Bed Simulator', *Engenharia Térmica*, no. 3, pp. 64–70.

Scala, F. 2013, *Fluidized Bed Technologies for Near-Zero Emission Combustion and Gasification*, Woodhead Publishing, Cambridge.

Sette, E., Pallarès, D. & Johnsson, F. 2014, 'Experimental evaluation of lateral mixing of bulk solids in a fluid-dynamically down-scaled bubbling fluidized bed', *Powder Technology*, vol. 263, pp. 74–80.

Solimene, R., Chirone, R. & Salatino, P. 2012, 'Characterization of the Devolatilization Rate of Solid Fuels in Fluidized Beds by Time-Resolved Pressure Measurements', *AIChE Journal*, vol. 58, no. 2, pp. 632–645.

de Souza-Santos, M.L. 1987, *Modelling and Simulation of Fluidized-Bed Boilers and Gasifiers for Carbonaceous Solids*, Department of Chemical Engineering and Fuel Technology, University of Sheffield.

de Souza-Santos, M.L. 2007, 'A new version of CSFB, comprehensive simulator for fluidised bed equipment', *Fuel*, vol. 86, pp. 1684–1709.

Spliethof, H. 2010, *Power Generation from Solid Fuels*, Springer-Verlag, Berlin.

VDI 2010, *VDI Heat Atlas*, 2nd edition, Springer-Verlag, Heidelberg.

Vun, S., Naser, J., Witt, P.J. & Yang, W. 2010, 'Measurements and numerical predictions of gas vortices formed by single bubble eruptions in the freeboard of a fluidised bed', *Chemical Engineering Science*, vol. 65, pp. 5808–5820.

Wen, C.Y. & Chen, L.H. 1982, 'Fluidized bed freeboard phenomena: Entrainment and elutriation', *AIChE journal*, vol. 28, no. 1, pp. 117–128.